JOURNAL OF THE GEOLOGICAL SURVEY OF BRAZIL

The Jurassic basaltic magmatism of the Tacutu rift-tye basin, Amazonian Craton, Brazil: A contribution to petrological studies

Steffanie Loislen de Sousa Oliveira[1], Valmir da Silva Souza[1*], Stélio Soares Tavares Junior[2], Reinhardt Adolfo Fuck[1]

[1]Geoscience Institute, University of Brasília, Brasília, Brazil.
[2]Geoscience Institute, Federal University of Roraima, Boa Vista, Brazil

Abstract

The Tacutu rift-type basin (on the border of Brazil and Guyana) is related to the initial opening of the Equatorial Atlantic Ocean during the Mesozoic. On the Brazilian side, during the pre-rift stage, basaltic magmatism (Apoteri Formation) associated with a fluvial-deltaic system took place within a magma-poor rift domain. At least two basaltic magmatic pulses have been recorded (Ap1 and Ap2). These rocks are basalt to basalt-andesite in composition, with subalkaline, tholeiitic to calc-alkaline, low-Ti CAMP (Central Atlantic Magmatic Province), and intra-plate geochemical signatures. However, Ap1 displays an aphanitic to fine-grained porphyritic texture, while Ap2 has a notable vesicular textural feature. Ap1 has low MgO, high Ti, Zr, and REE, while Ap2 has high Mg, low Ti, Zr, and REE. Geochemical and isotopic (low Nd and high Sr isotope ratios) indicators point to different rates of differentiation and crustal contamination between Ap1 and Ap2, probably related to crustal residence time. The variations in depth/depocenters, interior block architecture (horst-graben), and fault movement rates controlled the volume and emplacement moment of the basaltic magmatic pulses during the Tacutu rifting. On the Brazilian side, the Apoteri basaltic volcanism exhibited predominantly sub-aerial characteristics, with some degree of explosivity and fragmentation during the Ap2 pulse, associated with a fluvio-deltaic system. However, on the Guyana side, it is likely that this volcanism occurred with a significant submarine volcanism component, associated with a deltaic-marine system.

Article Information

Publication type: Research Papers
Received 28 January 2026
Accepted 14 April 2026
Online pub. 23 April 2026
Editor: Martin Roddaz

Keywords:
Amazonian craton
Tacutu rift
basaltic magmatism
Apoteri Formation
continental breakup

*Corresponding author
Valmir da Silva Souza
E-mail address:
vsouza@unb.br

ISSN: 2595-1939
https://doi.org/ 10.29396/jgsb.2026.v9.n2.4
Open access at https://jgsb.sgb.gov.br

1. Introduction

During continental rifting, the initial stages usually gather siliciclastic sedimentary sequences and basaltic magmatism as results of lithospheric extension related to mantle plume action (Ruppel 1995; Buck et al. 1999; Pirajno & Santosh 2015). Modern concepts on global tectonics propose different mechanisms to explain the evolution of the internal rift architecture on the extended lithosphere, whose tectonic fabrics control the ratios between the different volumes of sedimentation and magmatism produced (Corti 2012; Huismans & Beaumont 2014; Koptev et al. 2018; Zwaan et al. 2018). Therefore, the petrological investigation of basaltic magmatism provides indirect information about lithospheric extension rate, degree of crust-mantle interaction, chronology, and magmatic evolution during the pre- to syn-rift stages of the continental breakup (Lebedev et al. 2006; Giordano et al. 2014; Smets et al. 2016; Furman et al. 2016; Zhao et al. 2020).

The northernmost region of the Amazonian craton, at the border of Brazil and Guyana (Figure 1), hosts a rift-type linear tectonic feature named the Tacutu Basin (May 1971; Berrangé & Dearnley 1975). It is related to the Pangaea-Gondwana supercontinent breakup that led to the opening process of the Equatorial Atlantic Ocean during the Mesozoic (Crawford et al. 1985; Marzoli et al. 1999; McHone 2000; Biari et al. 2017; Loparev et al. 2021; Figueiredo et al. 2022). The Tacutu continental rift presents an internal architecture of the hemi-graben type, with the basaltic magmatism related to the pre- to syn-rift phases associated with fluvial-lacustrine sedimentary sequences (Marzolli et al. 1999; Eiras et al. 1994; Reis et al. 2006; Vaz et al. 2007). This basaltic magmatism has subaerial and local subaqueous features, a basalt to basaltic-andesite composition, with sub-alkaline and continental tholeiitic to calc-alkaline geochemical signatures, and is marked by at least two magmatic pulses (Vaz et al. 2007; Pinto et al. 2017; this paper). The available geochronological data by the K-Ar and Ar-Ar methods indicated ages between 200 and 150 Ma (Marzoli et al. 1999; Reis et al. 2006). However, based on U-Pb and Sm-Nd isotopic data from the Roraima Alkaline Province, Figueiredo et al. (2022) proposed that the basaltic floods related to the Tacutu extensional tectonic event occurred between 153 and 135 Ma.

In this paper, we present complementary petrography, geochemistry, Sm-Nd and Sr-Sr isotopic data, as well as unpublished data on mineral chemistry results on the basaltic magmatism of the Apoteri Formation, related to the pre- to syn-rift phase of the Tacutu Basin. The results permitted some petrological inferences about the emplacement geological setting and eruption mechanisms, as well as about the contamination rate during the rise through the crust stages.

Figure 1: A) Geographic location of the Tacutu continental rift on the border of Brazil and Guyana; B) Simplified regional geological map of the Mesozoic Tacutu Basin area on the Brazil side, indicating the sampling site of the Apoteri basaltic rocks (Modified from CPRM 2022); C) Simplified and schematic geological section of the Tacutu hemi-graben basin (adapted and modified from Reis et al. 1994).

2. Methods

The petrographic, mineral chemistry, and Sm-Nd isotopic analyses were carried out at the Geosciences Institute of the University of Brasília, while the Sr-Sr isotopic analyses were carried out at the Pará-Iso Isotope Geology Laboratory of the Federal University of Pará. The whole-rock geochemistry data were obtained in a commercial laboratory of the Australian Laboratory Services (ALS®).

The conventional petrography and mineral chemistry studies were performed on polished thin sections. For punctual mineral chemical analyses on pyroxene crystals, a JEOL® JXA-8230 Electron Probe Microanalyzer (EPMA) was used. The wavelength-dispersive system (WDS) operated with acceleration voltage of 15 kV, a beam current of 10 nA and counting time of 10 s. The standards used for calibration were natural and synthetic minerals: microcline (Si, Al and K), andradite (Fe and Ca), albite (Na), forsterite (Mg), vanadinite (V), pyrophanite (Ti and Mn), barite (Ba), synthetic Cr2O3 (Cr) and NiO (Ni), while the Ti and V analysis used the kα lines. Ferric and ferrous iron contents were calculated using Droop (1987). The analytical precision (expressed as relative standard deviation) is ± 1% for element concentrations >10 ppm and ±10% for concentrations <10 ppm.

The geochemical analysis used analytical instrumentation set applying ICP-OES to obtain major and minor elements and ICP-MS for traces and rare earth elements (REE). Lithium metaborate/tetraborate was added to the pulverized sample and then melted at 1000o C to form a melt that was cooled and dissolved in an acidic mixture containing nitric, hydrochloric and hydrofluoric acids. Loss on ignition (LOI) was determined using 1.0 g of sample previously weighted, heated at 1000o C for 1 h, cooled, and then weight again. The limit of detection (LOD) standardization method reached 0.01 % for major and minor elements, while for traces and REE the LOD ranged from 0.01 to 0.05%.

For Sm-Nd analysis, a Thermal Ionization Mass Spectrometry (TIMS) equipment was used, following the methodology described by Gioia & Pimentel (2000). Whole-rock powders (ca. 50 mg) were mixed with a 149Sm/150Nd spike solution and dissolved in Savillex capsules. Sm and Nd extraction of whole-rock samples followed conventional cation exchange techniques, using Teflon columns containing LN-Spec resin (di-(2-ethylhexyl) phosphoric acid (HDEHP) supported on PTFE powder. Sm and Nd samples were loaded on re-evaporation filaments of double filament assemblies and the isotopic measurements were carried out on a multi-collector Finnigan MAT 2.

For Sr-Sr analysis, a 0.5 ml-aliquot from the Sm-Nd solutions was directly loaded onto Teflon® columns containing approximately 83 mg of Eichrom® Sr-Spec resin (50–100 µm) to separate the Sr fraction from the matrix. Sr isotope measurements were performed using a Thermo Scientific TRITON™ Plus Thermal Ionization Mass Spectrometer (TIMS) operating in static multi-collector mode. The average 87Sr/86Sr obtained for the NBS-987 standard was 0.710257 ± 0.000007 (2σ; n = 9), consistent with the recommended 87Sr/86Sr = 0.71025 of the Thirlwall (1991), with the initial 87Sr/86Sr ratios/samples calculated using the 87Rb decay constant 1.393 × 10 -11 year -1 (Nebel et al. 2011).

3. Geological setting

The basement of the region between Brazil and Guyana (more specifically, the State of Roraima) is composed of variable and complex Paleo- to Mesoproterozoic lithologies, distributed within different tectonic and geochronological

domains. The Tacutu continental rift area is inserted in the northeastern portion of the so-called Central Guyana domain (CPRM 1999; Delor et al. 2003; Reis et al. 2003 and 2013; Santos et al. 2003; Almeida et al. 2007; Fraga et al. 2009).

In this place, the Mesoproterozoic basement has an anorthosite-mangerite-charnockite-rapakivi granite suite (AMCG-type), dated between 1.53 and 1.43 Ga, and inserted in the Mucajaí Intrusive Suite. The Paleoproterozoic basement brings together para- and orthogneiss, migmatites, metagranitoids, metavolcanics and metamafic-ultramafic rocks, with ages between 1.96 and 1.92 Ga, inserted in the Rio Urubu and Orocaima igneous belts. Aluminous paragneisses and calc-silicate rocks, metachert, ortho- and para-amphibolites, gondite, quartzite, and phyllite, dated between 2.05 and 1.91 Ga, and situated within the Cauarane Group, complete the Paleoproterozoic geological framework (CPRM 1999; Fraga 2002; Reis et al. 2003 and 2013; Fraga et al. 2009; Heinonen et al. 2012; CPRM 2022). In contrast, the Mesozoic Tacutu linear extensional structure has a SW-NE trend that extends about 300 km from Brazil to Guyana (Figure 1A), measuring between 30 and 50 km wide and more than 7 km in thickness, covering an area of about 12,500 km² (Eiras et al. 1994).

On the Brazilian side, the lithostratigraphy of the Tacutu continental rift is composed of regional units related to pre- to post-rift stages. The pre- to syn-rift stages are represented by the Apoteri and Manari formations. The magmatism studied here is inserted in the Apoteri Formation. It has a basaltic to basaltic-andesitic composition, sub-alkaline and continental tholeiitic to calc-alkaline geochemical signatures, and an estimated age between 200 and 135 Ma (Berrangé & Dearnley 1975; Marzolli et al. 1999; Reis et al. 2006; Pinto et al. 2017; Figueiredo et al. 2022, this paper). This magmatism has been interpreted as the result of the asthenospheric uplift related to the mantle plume during the opening of the Equatorial Atlantic Ocean in the Triassic-Jurassic, accompanied by fracturing and consumption of the lithosphere base. The produced basaltic magmatism invaded the lithosphere as dikes and sills, and ended with subaerial to subaqueous fissure flows in distinct moments, marked by the presence of vesicles, columnar jointing, and pillow lava features (Eiras & Kinoshita 1990; Eiras et al. 1994; Vaz et al. 2007; Pinto et al. 2017; Loparev et al. 2021; Figueiredo et al. 2022).

The Apoteri Formation is discordantly covered by the siliciclastic rocks of the Manari Formation, represented by siltstones, shales, and dolomitic lenses related to the lacustrine environment, with an inferred Lower Jurassic age (Eiras & Kinoshita 1990; Eiras et al. 1994). The transition between pre- and active rift stages is marked by crustal stretching with normal mega-faults (graben-horst) controlling the rifting architecture and generating depocenters. At this stage, halite and gypsum lenses interspersed with shales, siltstones, and pyrite marls of the Pirara Formation occur, followed by calciferous siltstones, sandstones, carbonates, and shales of the Tacutu Formation, finishing with arkosean sandstones of the Tucano Formation. This stage has been interpreted as a fluvial-deltaic system under arid to semi-arid climate conditions during the Late Jurassic to Early Cretaceous (Eiras & Kinoshita 1990; Eiras et al. 1994; Vaz et al. 2007; Castro et al. 2021).

In the Late Cretaceous, crustal stretching decreases and rifting stabilizes, but during the Miocene, transcurrent movements related to the convergent dynamics of the Cocos, Nazca, and Caribbean tectonic plates resulted in folds and inverse faults inside the Tacutu extensional structure (Eiras & Kinoshita 1988). Finally, in the post-rift stage, a thick siliciclastic sequence from the Neogene Boa Vista Formation, related to fluvial, lacustrine, and aeolian continental systems, covers the limits of the Tacutu continental rift and part of the basement rocks (CPRM 1999; Eiras et al. 1994; Milani & Thomaz Filho 2000; Reis et al. 2001; Menezes et al. 2020).

4. Local geology

On the Brazilian side, basaltic effusive flows and sills/dikes form the Apoteri Formation, observed mainly in small topographic elevations known as Serra Nova Olinda and Morro Redondo (Reis et al. 2006; Pinto et al. 2017). This paper presents only information regarding Serra Nova Olinda to the northwest of Boa Vitas city (Figure 1B), which has excellent exposures of the Apoteri basaltic magmatism, especially in the mining area for crushed basalt stone of the Granada Company (Figure 2A).

Two basaltic sub-horizontal lava flows are observed in this area (Figures 2B and 2C), confirming the reports by Pinto et al. (2017). The first lava flow (Ap1) is greenish gray in color and around 2 m thick. It has an aphanitic to fine porphyritic texture, marked by tabular plagioclase phenocrysts embedded in an aphanitic groundmass, containing frequent fractures/cavities filled with chalcedony and carbonates. In contrast, the second lava flow (Ap2) is dark green to greenish brown in color. It has around 1.5 m thick and covers Ap1, displaying vesicular texture marked by sub-rounded and irregular cavities (2-15 mm in size) embedded in an aphanitic to fine-grained porphyritic groundmass. These cavities normally are filled by zeolites, carbonates, and quartz/chalcedony. Vesicular coalescence features at the base of the Ap2 layer also are observed, favoring the formation of irregular centimetric cavities (Figure 2D).

Figure 2: Outcrops of the Apoteri basaltic rocks. A) Open pit mine for crushed basalt stone of the Granada Company; B) Field relationship between the two Apoteri basaltic lava flows; C) Geological contact detail between the two Apoteri basaltic lava flows; C) Vesicular enrichment and coalescence zone in the Ap2 basaltic lava flow.

5. Petrography

In general, the Apoteri (Ap1 and Ap2) rocks have plagioclase (An47-57) phenocrysts embedded in a fine-grained to aphanitic groundmass with an ophitic to sub-ophitic micro-texture. The euhedral to subhedral prismatic phenocrysts comprise less than 10% of the modal contents. They have between 0.5, 1 mm long, and a regular albite twinning, showing weak oscillatory zoning, with partial replacement by epidote, carbonate, and sericite as micro-aggregates. Occasionally, plagioclase phenocrysts may form glomeroporphyritic microtexture (Figures 3A and 3B). The groundmass consists mainly of random plagioclase laths in a mesh-like arrangement with interstitial subhedral crystals of clinopyroxene and olivine (0.3-0.6 mm in size), as well as scattered subhedral to anhedral crystals of ilmenite, magnetite, pyrite, apatite, quartz, and Fe-Ti oxi-hydroxides as accessory minerals. Clinopyroxene and olivine show different stages of replacement by tremolite-actinolite, chlorite, and serpentine

as micro-aggregates.

In addition, the cavities in the vesicular texture from Ap2 rocks have an internal zoning similar to geodes (Figures 3C and 3D), marked by a cortex-type external zone consisting mainly of microcrystalline chlorite, followed by zeolites, carbonates, chlorite, white mica, clay minerals, pyrite, and quartz/chalcedony in fibro-radial aggregates filling the central zone. Some cavities display vugs inside. Pinto et al. (2017) also report the presence of agate, opal, malachite, chalcopyrite, and bornite filling cavities.

Figure 3: Petrographic features of the Apoteri basaltic rocks. A) Ophitic to sub-ophitic common micro-texture marked by plagioclase phenocrysts embedded in fine-grained groundmass with interstitial clinopyroxene and olivine (Ap1 sample); B) Plagioclase phenocrysts in glomeroporphyritic micro-texture embedded in fine-grained groundmass (Ap1 sample); C) Vesicles embedded in an ophitic to sub-ophitic micro-texture. Note the size variation of the vesicles, which may indicate some degree of coalescence of the volatile phase (Ap2 sample); D) Detail of the internal mineral zonation of the vesicles in Ap2 sample (pl = plagioclase, cpx = clinopyroxene, ol = olivine, ch = chalcedony, cl = chlorite, zl = zeolite, wm = white mica, NX = crossed nicols, N// = parallel nicols).

6. Whole-rock and mineral chemistry

The Apoteri whole-rock geochemical data from the Ap1 and Ap2 samples presented in Table 1 are discussed below. The samples revealed important variations in the contents of major chemical elements (SiO2, Al2O3, Fe2O3, MgO, Na2O, K2O, CaO), as well as LOI, and with TiO2, MnO, and P2O5 ≤ 1%. These samples are relatively enriched in Ba, Sr, V, Cr, and Zr. Comparatively, the Ap1 samples have high Si (SiO2 = 51.9 - 54 wt.%), Ti (TiO2 = 1.24 - 1.36 wt.%), low Mg (MgO = 4.87 - 5.61 wt.%), and Mg# = 45.73 - 48.51, while the Ap2 samples have low Si (SiO2 = 50.10 – 51.30 wt.%), Ti (TiO2 = < 1 wt.%), high Mg (MgO = 7.21 - 7.32 wt.%) and Mg# = 57.09 - 59.04. In addition, the Ap1samples are relatively enriched in Nb, Ta, Th, Sn, U, Y, Hf, La and Ce. These geochemical characteristics agree with the data reported by Pinto (2017).

On the Na2O + K2O x SiO2 (TAS-type) classification diagram (Figure 4A), most Ap1 samples plot in the basaltic-andesite field, while AP2 samples plot in the basalt field, revealing a dominant subalkaline affinities. However, the SO-04 sample (AP2) has a slightly subalkaline affinity and plots very close to the alkaline-subalkaline transition field. Another sample from AP1 (SO-23) plots in the basaltic trachy-andesite field, indicating an alkaline affinity but close to the alkaline-subalkaline transition field. In contrast, On the Zr/TiO2 x Nb/Y classification diagram, the samples cluster between sub-alkaline basalt and basaltic andesite fields (Figure 4A). On the AFM classification diagram, Ap1 samples are distributed at the boundary between the tholeiitic and calc-alkaline series, while Ap2 shows a calc-alkaline affinity (Figure 4B). Variations in the contents of major and minor chemical elements may be related to several factors, including the differentiation and/or contamination rates during ascent and emplacement of magmas (Xia, 2014; Chin et al., 2018; Vermeesch and Pease, 2021).

Table 1: Whole-rock geochemistry of the Ap1 and Ap2 basaltic rocks from the Apoteri Formation.

Figure 4: Geochemical characteristics of the Ap1 and Ap2 basaltic rocks from the Apoteri Formation. A) Na2O + K2O x SiO2 and Zr/TiO2 x Nb/Y for volcanic rocks discriminant diagrams (Le Maitre et. al 1989 and Winchester & Floyd 1977); B) AFM discriminant diagram for tholeiitic and calc-alkaline fields (Irvine & Baragar 1971); C) TiO2 x FeOtot/MgO diagram indicating the CAMP-type continental flood basalts fields (Chabou et al. 2010); D) Zr/Y x Zr tectonic fields diagram (Pearce and Norry 1979); E) REEs-normalized pattern diagram (chondrite-normalized pattern of Boynton 1984); F) Multi-element spidergram pattern diagram. Note the comparison with the distribution pattern of the continental crust (MORB-normalized pattern of Saunders & Tarney 1984 with additions from Sun 1980); G-H) Nb/La x Nb and Ce/Pb x MgO discriminant diagrams applied to crustal contamination rates (Xia 2014; Furman 2007). Note the variation in MgO content leading to the formation of two groups of samples.

On the TiO2 x FeOtotal/MgO diagram, the Ap1 and Ap2 samples plot in the low-Ti CAMP field (Figure 4C), forming two groups with magmatic differentiation in different stages by fractional crystallization (Arbarede, 1992; Verati et al., 2005). Additionally, on the Zr/Y x Zr tectonic setting discriminant diagram, the Apoteri samples plot in the intra-plate basalts fields and form two distinct groups (Figure 4D). This geochemical signature is in accordance with the proposed geological and geotectonic setting for the Tacutu Basin rift (Reis et al. 2006; Pinto et al. 2017; Passos & Vidotti 2019).

In general, Ap1 and Ap2 samples have moderate to low normalized REE content and a similar distribution pattern, marked by low to moderate fractionation between LREE and HREE (Figure 4E), with LaN/SmN = 1.87 - 2.28 and GdN/YbN = 1.40 - 1.61, separated by a small anomaly in EuN (Eu/Eu* = 0.27 - 0.35). However, the Ap1 samples have a slightly higher normalized REE content (LaN + CeN = 77.12 – 89.82 and TmN + YbN = 23.64 – 28.68) compared to the Ap2 samples (LaN + CeN = 54.18 - 62.05 and TmN + YbN = 19.31 – 20.58). On the MORB-normalized multi-element diagram, all samples (Ap1 and Ap2) are relatively enriched in LILE (K, Rb, Ba) and depleted in HFES (Ce, P, Zr, Hf, Ti, Y, Yb), showing positive Rb and Nb anomalies, and negative Sr, Ta, P, and Ti anomalies (Figure 4F). It is also possible to observe that the Ap1 samples show a slightly higher normalized HFES content. In general, the distribution pattern shown by samples is similar to the average pattern of the upper continental crust, indicating their continental natures. Usually, variations in the normalized REE and HFSE contents have been attributed to fractionation or differentiation rates (Xia 2014; Haissen et al., 2021; Doucet et al., 2022; Heinonen et al., 2022). Apoteri samples (AP1 and Ap2) are marked by higher Zr (> 70 ppm), lower Nb (8-5 ppm), lowers Nb/La, La/Ba, Th/Yb, Ce/Pb ratios (Figures 4G-H), and HFES depletions. Such geochemical characteristics have been established for basaltic rocks that have undergone some degree of mantle-crust contamination (Hofmann et al., 1986; Kieffer et al, 2004; Furman 2007; Haissen et al., 2021; Xia 2014).

On the Fenner-type diagrams, the MgO content was applied as a differentiation index, revealing two groups of rocks (Ap1 and Ap2): a group with high TiO2 and low MgO, and another group with low TiO2 and high MgO (Figure 5). Overall, SiO2, Fe2O3, Y, and La contents tend to decrease with increasing MgO, while Al2O, Sr, and Cr have a positive correlation with MgO, indicating the important role of the iron-magnesium minerals, magnetite/ilmenite, and feldspar fractionations during magmatic crystallization. This trendy is most noticeable in rocks from the Ap1 group, which contain a large amount of

Fe-Ti oxy-hydroxide minerals. Additionally, applying the Zr as a geochemical index, a positive linear correlation with TiO2 is noted, and two groups of rocks are again formed: a group with low Zr and TiO2, and another group with high Zr and TiO2 (Figure 6). Other low mobility elements, such as Y, Th, Nb, Hf, and La, also presented a positive correlation with Zr, demonstrating the incompatible behavior for these elements. In contrast, Sr and Cr presented a negative correlation with Zr, indicating their compatible behavior in relation to the feldspar, pyroxene, and olivine fractionation degree. Some of these geochemical characteristics also agree with the data reported by Pinto (2017).

Figure 5: Fenner-type element variation diagrams of the Ap1 and Ap2 basaltic rocks from the Apoteri Formation. Selected major and trace elements versus MgO.

Figure 6: Zr versus selected major and trace elements diagrams applied for possible evaluation of the geochemical mobility of elements in the Ap1 and Ap2 basaltic rocks from the Apoteri Formation.

In addition, chemical composition studies of Fe-Mg aluminum silicates (pyroxene, amphibole, olivine, and biotite) have been widely applied as some indicators in the geochemical, thermobarometer, and tectonic setting of mafic-ultramafic rocks (e.g., Zhang et al. 2018; Das et al. 2020; Wang et al. 2021). In this paper, the mineral chemistry studies were carried out on clinopyroxene crystals from the Ap1 rocks, whose results are shown in Table 2. On the Fs-Wo-En ternary classification diagram, the representative Ca–Fe–Mg clinopyroxene analyses (WDS) plot in the Ti-augite field (Figure 7A). On the Ti x Ca + Na and Ti + Cr x Ca atomic correlation diagrams, the analyzed spots plot in the tholeiitic and calc-alkali basalts and non-orogenic basalts, respectively (Figures 7B-C), also indicating their chemical affinity with continental basaltic magmatism.

Table 2: Electron microprobe analysis and representative structural formula of clinopyroxene from Ap1 pulse of the Apoteri Formation.

Figure 7: Pyroxene mineral chemistry diagrams applied to the Apoteri basaltic rocks. A) Mineral chemistry plot in Ca–Mg–Fe pyroxenes in the Fs-Wo-En ternary diagram (after Morimoto et al., 1988); B and C) Tectonic discriminant diagrams based on mineral chemistry. Note that analyzed spots plot on the tholeiitic and non-orogenic basalts fields, respectively (adapted from Leterrier et al., 1982).

7. Sm-Nd and Sr-Sr isotopic geology

Whole-rock Sm-Nd and Sr-Sr isotopic data listed in Tables 3-4 are discussed below. Due to uncertainties regarding the crystallization age of the Apoteri Formation, which vary between 200 and 150 Ma (Berrangé & Dearnley 1975; Marzolli et al. 1999; Reis et al. 2006; Pinto et al. 2017), we apply the average age of 175 Ma as a reference to calculate the ƐNd (t = 0.17 Ga).

Table 3: Whole-rock Sm–Nd isotopic data of the basaltic rocks of the Apoteri Formation.

Table 4: Whole-rock Sr–Sr isotopic data of the basaltic rocks of the Apoteri Formation.

In general, the samples show an initial 143Sm/144Nd ratio = 0.512374 - 0.512464 and f Sm/Nd between -0.24 and -0.25. Similar 143Nd/144Nd values (0.5122238 - 0.512311) for the Apoteri magmatism are also reported by Pinto et al. (2020). However, the Ap1 lava flow has ƐNd (0) from -3.40 to -3.75, ƐNd (t = 0.17) from -2.36 to -2.58, and Nd TDM model age = 1.33 - 1.35 Ga, while the Ap2 lava flow has ƐNd (0) between -4.66 and -5.16, ƐNd (t = 0.17) from -3.71 to -4.17, and Nd TDM model age = 1.53 - 1.54 Ga. The ƐNd versus time diagram summarizes the Nd evolution patterns provided by the samples investigated (Figure 8A) and indicates varying degrees of interaction/contamination with the Paleoproterozoic sialic crust.

All samples showed high initial 87Sr/86Sr isotopic ratio, indicating the important role of the crust-mantle interaction process during magmatic emplacement. The Ap1 samples have 87Sr/86Sr(0) ratio = 0.711179 - 0.714475, with 87Sr/86Sr(t = 175 Ma) ratio = 0.70972 – 0.71155, while the Ap2 samples have 87Sr/86Sr(0) ratio = 0.713113 - 0.714820 and 87Sr/86Sr(t = 175 Ma) ratio = 0.71185 – 0.71345. However, according to Pinto et al. (2020), the Apoteri basalts have 87Sr/86Sr ratio = 0.70758 - 0.708948. The variations in the Sr isotopic ratio values observed in the different studies suggest basaltic rocks with different rates of crustal contamination, probably related to different outcrops or sampling locations.

On the 143Nd/144Nd x 87Sr/86Sr(t = 175 Ma) diagram (Figure 8B), the samples plot along a trend towards the field of rocks with a higher rate of mantle-crust interaction/contamination, marked by low Nd and high Sr isotope ratios. On ƐNd(t = 175 Ma) x 87Sr/86Sr(t = 175 Ma) diagram (Figure 8B), the samples show a good isotopic correspondence with the low-Ti basalts to andesitic basalts of the Central Atlantic Magmatic Province (CAMP), plot close to the EM-II mantle pole, and indicate that the Ap1 samples have a lower rate of crustal contamination compared to the Ap2 samples.

Figure 8: Nd and Sr isotope ratios characteristics of basaltic rocks of the Apoteri Formation. A) ƐNd x Age (Ga) evolution patterns diagram applied to basaltic rocks of the Apoteri Formation. Depleted mantle (DM) curve according to DePaolo (1981); B) 143Nd/144Nd x 87Sr/86Sr and ƐNd x 87Sr/86Sr associated diagrams with time (t) back-calculated to 175 Ma, indicating the important role of mantle-crust interaction/contamination rate and the isotopic correspondence with low-Ti CAMP basalts. The CAMP field with Nd and Sr isotopes ratios back-calculated to 200 Ma, according to Deckart et al. (2005).

8. Discussion

The Pangaea-Gondwana supercontinent fragmentation geodynamics, followed by the opening and expansion stages of the Equatorial Atlantic Ocean during the Mesozoic, favored the formation of a set of linear extensional structures (rift zones) oblique to the main direction of fragmentation (Burke, 1976; White & McKenzie, 1989; Bonatti 1996; Lamotte et al., 2015; Peace et al., 2020). Records of these continental geodynamics can be found in northern Brazil, Venezuela, Guyana, Suriname, and northwest Africa (Matos, 2000; De Min et al., 2003; Deckart et al., 2005; Heine and Brune, 2014; Loparev et al. 2021; Guan et al., 2021). On the border between Brazil and Guyana, the Tacutu rift-type basin is a result of this oblique continental segmentation during the opening of the Equatorial Atlantic. Its internal geodynamics, controlled by a normal fault system (horst-graben blocks), favored the dike, sill, and subaerial to subaqueous fissure basaltic flows related

to the Apoteri magmatism (Eiras and Kinoshita, 1990; Eiras et al., 1994; Vaz et al., 2007; Thomaz Filho et al. 2000; Pinto et al., 2017; Marzolli et al., 2018; Loparev et al., 2021; Figueiredo et al., 2022).

On the Brazilian side, at least two basaltic to basaltic-andesite pulses have been recorded (Ap1 and Ap2). These rocks have a dominant subalkaline affinity, with low-Ti CAMP and intra-plate geochemical signatures (Pinto et al., 2017; in this paper). However, one AP1 sample showed alkaline affinity or close to the alkaline-subalkaline transition line, suggesting a possible coexistence between alkaline and subalkaline magmas. In general, alkaline intra-plate basalts are common, but the coexistence between alkaline (silica-undersaturated) and sub-alkaline (silica-saturated) intra-plate basalts can occur, which has been primarily attributed to heterogeneity mantle source or variations in the crust-mantle interaction rate (Chen et al. 1991; Cook et. al, 2005; Wang and Liu, 2021; Wilson et. al, 2025).

In addition, these rocks have lower Nb/La, La/Ba, Th/Yb, and Ce/Pb ratios, indicating a considerable degree of crustal contamination (Hofmann et al., 1986; Kieffer et al, 2004; Xia 2014; Pinto et al., 2017). The initial Nd and Sr isotopic ratios also reveal important crustal participation, marked by the Mesoproterozoic Nd TDM (1.54 - 1.33 Ga) model age, negative ƐNd values (-3.40 to -4.17), and the highest and variable 87Sr/86Sr ratio (0.70972 to 0.71345), indicating different crust-mantle interaction rates. In general, Triassic-Jurassic low-Ti CAMP basalts from Atlantic equatorial margin have low Nd and high Sr isotope ratios, high LILE, low HFES, and variable degree of crustal contamination (Fodor et. al, 1990; Bertrand, 1991; De Min et al., 2003; Deckart et al., 2005; Verati et al., 2005; Merle et al., 2014; Marzoli et al., 2018). In this geological setting, primitive magmatic rocks are rare or absent, and the vast majority of CAMP-type basalts have sources with significant participation of the metasomatized sub-continental lithospheric mantle - SCLM (Merle et al., 2014; Marzoli et al., 2018; Pinto et al. 2017). Furthermore, the crust-mantle interaction rates, related to the partial assimilation within crustal magma chambers or during rise to the surface, also interfered with the primitive geochemistry and isotopic signatures.

From a comparative perspective, Ap1 has low MgO and high Ti, Zr. and REE, while Ap2 has high Mg and low Ti, Zr and REE, suggesting some variation in magmatic differentiation stages. Probably related to the fractional crystallization rate and consequent variations in the Fe-Ti minerals content, as well as metasomatic influence and thermodynamic constraints, for example (Chabou et al. 2010; Chistyakova and Latypov, 2012; Krans et al., 2024). However, Ap1 proved to be a more differentiated magmatic phase or one with a higher fractional crystallization rate, likely resulting from a longer crustal residence time during the initial stages of the Tacutu rifting process.

Ap2 has a high vesicle content, which may be the result of several petrogenetic factors, including variations in decompression rate, viscosity, melting temperature, and rheology of multiphase magmas (Bottinga & Javoy 1990; Saar & Manga 1999; Mader et al. 2013; Soldati et al. 2020). In this context, morphological, statistical, and chemical studies on vesicles in basaltic lava flows have been applied, for example, to determine the explosivity degree at the time of eruption (Mangan et al., 1993; Houghton & Gonnermann, 2008; Hashimoto & Sumita, 2021; Colombier et al., 2021). Therefore, complementary studies on the vesicular Ap2 lava flow would be a good opportunity to make inferences about the eruptive mechanism.

On the other hand, variations in decompression rates caused by rapid volume changes, related to space generation during fault movements within a volcanic conduit, can influence magma properties, specifically its geochemistry, viscosity, fragmentation (bubbles), and overall explosivity (Jaupart. 1996; Fiege et al., 2015; Barth et al., 2019; Allison et al. 2021). Therefore, it is probable that extensional geodynamics within the Tacutu Basin may have an important role in the magma channeling and eruptive styles, influencing the rheology of the Ap1 and Ap2 lava flows, for example. However, this hypothesis requires further studies, also becoming a good opportunity for the application of temperature-pressure experiments (numerical models) to the mineralogy and geochemistry of the Apoteri basaltic magmas.

Previous geophysical investigations revealed that the Mesozoic Tacutu Basin internal geometry has greater depth on the Guyana side (from 3000 to 5400 m), marked by the dominance of the deltaic-marine system. In contrast, on the Brazil side, the depth varies from 600 to 3000 m, with the predominance of the fluvial-deltaic system (Crawford et al. 1985; Mariak 2003; Passos & Vidotti 2019; Webster et al. 2020). The Figure 9 is a simplified hypothetical illustration of the mantle-derived magma recharge and eruption moments for the Ap1 and Ap2 lava flows, with the volcanism from fissure zones controlled by the fault movements of the Tacutu Basin rifting. On the Brazilian side, dikes, sills, and sub-aerial fissure eruptions likely predominated, with linear vents, lava flows, and variable explosive potential. However, on the Guyana side, it is likely that the eruptive activities had some significant subaqueous volcanic component.

Figure 9: A simplified geological model proposed for the emplacement moments of the Apoteri Ap1 (A) and Ap2 (B) basaltic lava flows during the Tacutu pre-rift phase (early Jurassic). The Tacutu rift internal geometry favored sub-aerial fissure basaltic volcanism with some degree of explosivity in the Ap2 pulse, associated with a fluvial-deltaic system on the Brazilian side, as well as underwater fissure volcanism associated with deltaic-marine systems on the Guyana side.

Finally, K-Ar and Ar-Ar geochronological data available point to these basaltic magmatism ages between 200 and 150 Ma (Marzoli et al. 1999; Reis et al. 2006). However, due to the rarity of zircon crystals in the Apoteri basalts, we are applying the whole-rock chemical dissolution technique (e.g., Oliveira et al. 2022) in order to obtain crystals suitable for the U-Th-Pb method, which could provide a more precise age.

9. Conclusions

The petrological data presented in this paper corroborate, in part, the available data on the Lower Jurassic basaltic magmatism of the Apoteri Formation, which leads us to the following conclusions.

During the Tacutu Basin pre- to syn-rift phase, on the Brazilian side, at least two basaltic lava flows (Ap1 and Ap2), related to the Equatorial Atlantic Ocean opening, can be identified. These rocks have from basalt to basalt-andesite composition, dominant subalkaline, low-Ti CAMP, and intra-plate geochemical signatures. Field relationships, supported

by geochemistry and isotopic geology data, indicate that Ap1 and Ap2 lava flows are probably related to the same event, although with mantle-derived magma recharge at distinct moments during the short lithospheric extent of the Tacutu Basin rifting.

The rifting extensional geodynamics likely played an important role in the magma recharge mechanism, especially during the space generation, also interfering with the decompression and fragmentation rates, as well as with the fissure volcanism style. Consequently, some geochemistry and isotopic (Nd and Sr) variations related to crystallization thermodynamics were then generated. Ap1 shows greater differentiation by fractional crystallization, likely related to higher crustal residence during the initial stages of the Tacutu rifting process. Additionally, variation in Nd and Sr isotope ratios between Ap1 and Ap2 also indicates different crustal contamination rates during the magma rise through the crust at distinct moments. Finally, the high vesicle content in Ap2 suggests accelerated decompression during fault displacement, leading to magma fragmentation and some explosivity.

Despite recent advances in the petrogenetic understanding of this basaltic magmatism in the Tacutu Basin, further experimental petrological studies (barometry and thermometry) on these magmatic dynamics are still needed. We believe that the excellent outcrops of the Apoteri Formation in the Serra Nova Olinda (Boa Vista city) could serve as laboratories for these investigations.

Acknowledgments

This research was financially supported by the INCT - Brazil Tectonic Studies (CNPq, CAPES, FAPDF) and FAP-DF-Brazil (project no. 193.001.263/2017), as well as by CAPES-Brazil in granting a scholarship to S.L.S. Oliveira (first author). The authors are grateful to the Geology Postgraduate Program of the Geoscience Institute, University of Brasília, for laboratory and technical staff support. Gratitude to Dr. Jussi S. Heinonen (Abo Akademi University, Finland) for the first review of the manuscript, which led us to a significant revision and improvement for a new version. We would also like to thank the Granada Mining Company and the Federal University of Roraima for their support in the fieldwork. R.A. Fuck acknowledges the CNPq research fellowship. Finally, we thank the review and editorial team of the Journal of the Geological Survey of Brazil for their criticisms and suggestions that improve the manuscript.

References

Albarede F., 1992. How deep do common basaltic magmas form and differentiate? Journal of Geophysical Research, 97(B7):10.997-11.009.

Allison C.M., Roggensack K., Clarke A.B. 2021. Highly explosive basaltic eruptions driven by CO2 exsolution. Nature Communications, 12:2017, https://doi.org/10.1038/s41467-020-20354-2

Almeida M.E., Macambira M.J.B., Oliveira E.C., 2007. Geochemistry and zircon geochronology of the I-type high-K calc-alkaline and S-type granitoid rocks from southeastern Roraima, Brazil: Orosirian collisional magmatism evidence (1.97-1.96 Ga) in central portion of Guyana Shield. Precambrian Research, 155(1–2):69–97, https://doi.org/10.1016/j.precamres.2007.01.004

Barth A., Newcombe M., Plank T., Gonnermann H., Hajimirza S., Soto G.J., Saballos A., Hauri E., 2019. Magma decompression rate correlates with explosivity at basaltic volcanoes — Constraints from water diffusion in olivine. Journal of Volcanology and Geothermal Research, 387:106664, doi:10.1016/j.jvolgeores.2019.106664

Berrangé J. P. & Dearnley R., 1975. The Apoteri volcanic formation - tholeiitic flows in the North Savannas Graben of Guyana and Brazil. Geologische Rundschau, 64:883–899.

Bertrand, H., 1991. The Mesozoic tholeiitic province of northwest Africa: a volcano-tectonic record of the early opening of Central Atlantic. In: Kampunzu, A.B., Lubala, R.T. (Eds.), Magmatism in Extensional Structural Settings. The Phanerozoic African Plate. Springer-Verlag, pp. 147-191.

Biari Y., Klingelhoefer F., Sahabi M., Funck T., Benabdellouahed M., Schnabel M., Reichert C., Gutscher M. A., Bronner A., Austin J. A., 2017. Opening of the central Atlantic Ocean: Implications for geometric rifting and asymmetric initial seafloor spreading after continental breakup. Tectonics, 36(6):1129–1150. https://doi.org/10.1002/2017TC004596

Bonatti E., 1996. Anomalous opening of the Equatorial Atlantic due to an equatorial mantle thermal minimum. Earth and Planetary Science Letters, 143:147-160.

Bottinga Y. & Javoy M., 1990. MORB degassing Bubble growth and ascent. Chemical Geology, 81:255-270.

Boynton W.V., 1984. Cosmochemistry of the rare earth elements: meteorite studies. In: Henderson, P. (Ed.), Rare Earth Element Geochemistry. Elsevier, pp. 63–114.

Buck, W.R., Lavier, L.L., Poliakov, A.N.B., 1999. How to make a rift wide. Philosophical Transactions of the Royal Society, A-357:671-693, http://dx.doi.org/10.1098/rsta. 1999.0348.

Burke K., 1976. Development of graben associated with the initial ruptures of the Atlantic Ocean. Tectonophysics, 36:93–112.

Campbell I.H., 2001. Identification of ancient mantle plumes. Geological Society of America, Special paper, 352:5-21.

Castro H., Giorgioni M., Souza V., Ramos M., Feitoza L. M., Dino R., Arienzoli L., 2021. Facies analysis, petrography, and palynology of the Pirara Formation (Upper Jurassic-Lower Cretaceous) - Tacutu Basin (Roraima, Brazil). Journal of South American Earth Sciences, 112:103574. https://doi.org/10.1016/j.jsames.2021.103574

Chabou M.C., Bertrand H., Sebai A., 2010. Geochemistry of the Central Atlantic Magmatic Province (CAMP) in south-western Algeria. Journal of African Earth Sciences, 58:211–219, doi:10.1016/j.jafrearsci.2010.02.009

Chen C.Y., Frey F.A., Garcia M.O., Dalrymple G.B., Hart S.R., 1991. The tholeiite to alkalic basalt transition at Haleakala Volcano, Maui, Hawaii. Contributions to Mineralogy and Petrology, 106:183-200.

Chin E.J., Shimizu K., Bybee G.M., Erdman M.E., 2018. On the development of the calc-alkaline and tholeiitic magma series: A deep crustal cumulate perspective. Earth and Planetary Science Letters, 482:277-287, doi:10.1016/j.epsl.2017.11.016.

Chistyakova S. & Latypov R., 2012. Magma differentiation and crystallization in basaltic conduits by two competing petrogenetic processes. Lithos, 148:142-161, doi:10.1016/j.lithos.2012.06.011

Colombier M., Vasseur J., Houghton B.F., Cáceres F., Scheu B., Kueppers U., Thivet S., Gurioli L., Montanaro C., Soldati A., Di Muro A., Dingwell D.B., 2021. Degassing and gas percolation in basaltic magmas. Earth and Planetary Science Letters, 573:117134, http://creativecommons.org/licenses/by-nc-nd/4.0/

Cook C., Briggs R.M., Smith I.E.M, Maas R., 2005. Petrology and geochemistry of intra-plate basalts in the South Auckland volcanic field, New Zealand: Evidence for two coeval magma suites from distinct sources. Journal of Petrology, 46(3):473-503, doi:10.1093/petrology/egh084.

Corti G., 2012. Evolution and characteristics of continental rifting: Analog modeling-inspired view and comparison with examples from the East African Rift System. Tectonophysics, 522–523 (1):1–33, https://doi.org/10.1016/j.tecto.2011.06.010

Corti, G., Bonini, M., Conticelli, S., Innocenti, F., Manetti, P., Sokoutis, D., 2003. Analogue modelling of continental extension: a review focused on the relations between the patterns of deformation and the presence of magma. Earth-Science Reviews 63, 169–247.

CPRM, 1999. Projeto Roraima Central (folhas NA.20-X-B e NA.20-X-D inteiras e parte das folhas NA.20-X-A, NA.20-X-C, NA.21-V-A e NA.21-V-C). Programa Levantamentos Geológicos Básicos do Brasil, Escala 1:500.000, CPRM, Manaus, 52p.

CPRM, 2022. Levantamentos geológicos e integração geológica regional do Estado de Roraima, mapa geológico - escala 1:1.000.000. Programa Geologia, Mineração e Transformação Mineral, MME, Serviço Geológico do Brasil – CPRM, Brasília.

Crawford F. D., Szelewski C. E., Alvey G. D., 1985. Geology and exploration in the Takutu graben of Guyana Brazil. Journal of Petroleum Geology, 8(1):5-36.

Das S., Goswami,B., Bhattacharyya C., 2020. Physico-chemical conditions of crystallization and composition of source magma of the Grenvillian post-collisional mafic–ultramafic rocks in the Chhotanagpur Gneissic Complex, Eastern India. Journal of Earth System Science, 129(1). https://doi.org/10.1007/s12040-019-1313-4

Deckart k., Bertrand H., Liégeois J-P., 2005. Geochemistry and Sr, Nd, Pb isotopic composition of the Central Atlantic Magmatic Province (CAMP) in Guyana and Guinea. Lithos, 82:289-314, doi:10.1016/j.lithos.2004.09.023

Delor, C., Lahondere, D., Egal, E., Lafon, J.-M., Cocherie, A., Guerrot, C., Rossi, P., Truffert, C., Theveniaut, H., Phillips, D., Avelar, V.G. de, 2003. Transamazonian crustal growth and reworking as revealed by the 1:500,000-Scale geological map of French Guiana. Geologie de la France, (2-4):5-57.

De Min A., Piccirillo E.M., Marzoli A., Bellieni G., Renne P.R., Ernesto M., Marques L.S., 2003. The Central Atlantic Magmatic Province (CAMP) in Brazil: Petrology, Geochemistry, 40Ar/39Ar Ages, Paleomagnetism and Geodynamic Implications. In The Central Atlantic Magmatic Province: Insights from Fragments of Pangea. Geophysical Monograph Series, 136:91-128, doi:10.1029/136GM06.

DePaolo, D., 1981. Neodymium isotopes in the Colorado front range and crust-mantle evolution in the proterozoic. Nature, 291:193-196.

Dostal J. & Durning M., 1998. Geochemical constraints on the origin and evolution of early Mesozoic dikes in Atlantic Canada. European Journal of Mineralogy, 10:79–93

Doucet L.S., Tetley M.G., Li Z-X, Liu Y., Gamaleldien H., 2022. Geochemical fingerprinting of continental and oceanic basalts: A machine learning approach. Earth-Science Reviews, 233:104192, https://doi.org/10.1016/j.earscirev.2022.104192.

Droop G.T.R., 1987. A general equation for estimating Fe+3 concentrations in ferromagnesian silicates and oxides from microprobe analyses using stoichiometric criteria. Mineral Magazine, 51: 431-435

Dupuy C. & Dostal J., 1984. Trace element geochemistry of some continental tholeiites. Earth and Planetary Science Letters, 67:61-69.

Dupuy C., Liotard J. M., Dostal J., 1992. Zr/Hf fractionation in intraplate basaltic rocks: carbonate metasomatism in the mantle source. Georhimica et Cosmochimica Acta, 56:2417-2423.

Ebinger C.J. & Casey, M. 2001. Continental breakup in magmatic provinces: An Ethiopian example. Geology 29, 527–530.

Eiras, J.F. & Kinoshita, E.M., 1988. Evidências de movimentos transcorrentes na Bacia do Tacutu. Boletim de Geociências da Petrobrás, Rio de Janeiro, 2(2/4):193-208.

Eiras, J.F. & Kinoshita, E.M., 1990. Geologia e perspectivas petrolíferas da Bacia do Tacutu. In: Gabaglia, G.P.R. & Milani, E. J (Eds.), Origem e evolução de bacias sedimentares, Petrobras, Rio de Janeiro, pp. 197-220.

Eiras J.F., Kinoshita E.M., Feijó F.J., 1994. Bacia do Tacutu. Boletim de Geociências da Petrobras, Rio de Janeiro, 8(1):83-89.

Fiege A., Vetere F., Iezzi G., Simon A., Holtz F., 2015. The roles of decompression rate and volatiles (H2O + Cl ± CO2 ± S) on crystallization in (trachy-) basaltic magma. Chemical Geology, 411:310-322, doi: 10.1016/j.chemgeo.2015.07.016

Figueiredo R.F., Azzone R.G., Santos T.J.S., 2022. The Roraima Alkaline Province: A cretaceous alkaline province in the Amazonian Craton. Geochemistry, 82:125900, https://doi.org/10.1016/j.chemer.2022.125900

Floyd P.A., & Winchester J.A., 1975. Magma type and tectonic setting discrimination using immobile elements. Earth and Planetary Science Letters, 27(2):211–218.

Fodor R.V., Sial A.N., Mukasa S.B., McKee E.H., 1990. Petrology, isotope characteristics, and K-Ar ages of the Maranhão, northern Brazil, Mesozoic basalt province. Contribution to Mineralogy and Petrology, 104:555-567.

Fraga L.M.B., 2002. A associação anortosito-mangerito-granito rapakivi (AMG) e suas encaixantes paleoproterozoicas: evolução estrutural, geocronologia e petrologia. Tese de Doutorado, Centro de Geociências, Universidade Federal do Pará, 351p.

Fraga L.M.B., Dall'Agnol R., Costa J.B.S., Macambira M.J.B., 2009. The Mesoproterozoic Mucajaí anorthosite-mangerite-rapakivi granite complex, Amazonian craton, Brazil. Canadian Mineralogist, 47(6):1469–1492, https://doi.org/10.3749/canmin.47.6.1469

Franke D., 2013. Rifting, lithosphere breakup and volcanism: comparison of magma-poor and volcanic rifted margins. Marine and Petroleum Geology 43:63-87, http://dx.doi.org/10.1016/j.marpetgeo.2012.11.003

Furman T., 2007. Geochemistry of east African rift basalts: an overview. Journal African Earth Sciences 48 (2–3), 147–160. https://doi.org/10.1016/j.jafrearsci.2006.06.009.

Furman T., Nelson W. R., Elkins-Tanton L. T., 2016. Evolution of the East African rift: Drip magmatism, lithospheric thinning and mafic volcanism. Geochimica et Cosmochimica Acta, 185:418–434. https://doi.org/10.1016/j.gca.2016.03.024

Gioia S.M.C.L. & Pimentel M.M., 2000. The Sm-Nd Isotopic Method in the Geochronology Laboratory of the University of Brasília. Anais da Academia Brasileira de Ciências, 72(2):219–245.

Giordano F., D'Antonio M., Civetta L., Tonarini S., Orsi G., Ayalew D., Yirgu G., Dell'Erba F., Di Vito M. A., Isaia R., 2014. Genesis and evolution of mafic and felsic magmas at Quaternary volcanoes within the Main Ethiopian Rift: Insights from Gedemsa and Fanta'Ale complexes. Lithos, 188:130–144. https://doi.org/10.1016/j.lithos.2013.08.008.

Guan H., Geoffroy L., Xu M., 2021. Magma-assisted fragmentation of Pangea: Continental breakup initiation and propagation. Gondwana Research, 96:56-75, doi:10.1016/j.gr.2021.04.003.

Haissen F., Zaghloul M.N., Dilek Y., Gimeno-Vives O., Mohn G., Cambeses A., Lamotte D.F., Bosse V., 2021. Geochemistry and Petrogenesis of Lower Jurassic Mafic Rock Suites in the External Rif Belt, and Chemical Geodynamics of the Central Atlantic Magmatic Province (CAMP) in Northwest Morocco. Journal of Geology, 129(5): 563-593, https://doi.org/10.1086/716499.

Hashimoto K. & Sunita I., 2021. Excitation of airwaves by bubble bursting in suspensions: regime transitions and implications for basaltic volcanic eruptions. Earth, Planets and Space, 73:143 https://doi.org/10.1186/s40623-021-01472-7

Heine C. & Brune S., 2014. Oblique rifting of the equatorial Atlantic: why there is no Saharan Atlantic Ocean. Geology, 42(3):211–214, https://doi.org/10.1130/G35082.1

Heine C., Zoethout J., Müller R.D., 2013. Kinematics of the South Atlantic rift. Solid Earth, 4(2): 215–253. https://doi.org/10.5194/se-4-215-2013

Heinonen A.P., Fraga L.M., Rämö O.T., Dall'Agnol R., Mänttäri I., Andersen T., 2012. Petrogenesis of the igneous Mucajaí AMG complex, northern Amazonian craton - Geochemical, U-Pb geochronological, and Nd-Hf-O isotopic constraints. Lithos, 151:17–34, https://doi.org/10.1016/j.lithos.2011.07.016

Heinonen J.S., Brown E.L., Turunen S.T., Luttinen A., 2022. Heavy Rare Earth Elements and the Sources of Continental Flood Basalts. Journal of Petrology, 63(10):1-17.

Herd R.A. & Pinkerton H., 1997. Bubble coalescence in basaltic lava: Its impact on the evolution of bubble populations. Journal of Volcanology and Geothermal Research, 75:137–157.

Hofmann A.W., Jochum K.P., Seufert M., White W.M., 1986. Nb and Pb in oceanic basalts: new constraints on mantle Evolution. Earth and Planetary Science Letters, 79:33-45.

Houghton B.F. & Gonnermann H.M., 2008. Basaltic explosive volcanism: Constraints from deposits and models. Chemie der Erde Geochemistry, 68:117-140, doi:10.1016/j.chemer.2008.04.002

Hui H., Niu Y., Zhidan Z., Huixin H., Dicheng Z., 2011. On the enigma of Nb-Ta and Zr-Hf fractionation-A critical review. Journal of Earth Science, 22(1), 52–66, https://doi.org/10.1007/s12583-011-0157-x

Huismans R. S. & Beaumont C., 2014. Rifted continental margins: The case for depth-dependent extension. Earth and Planetary Science Letters, 407: 148–162, https://doi.org/10.1016/j.epsl.2014.09.032

Iacumina M., De Mina A., Piccirilloa E.M., Bellieni G., 2003. Source mantle heterogeneity and its role in the genesis of Late Archaean–Proterozoic (2.7-1.0 Ga) and Mesozoic (200 and 130 Ma) tholeiitic magmatism in the South American Platform. Earth-Science Reviews 62:365-397, doi:10.1016/S0012-8252(02)00163-0

Irvine T.N. & Baragar W.R.A., 1971. A guide to the chemical classification of the common volcanic rocks. Canadian Journal of Earth Sciences, 8(5): 481-497, https://doi.org/10.1139/e71-055

Jaupart C., 1996. Physical models of volcanic eruptions. Chemical Geology, 128:217-227.

Khogenkumar S., Singh A.K., Singh R.K.B., Khanna P. P., Singh N. I., Singh W. I., 2016. Coexistence of MORB and OIB-type mafic volcanics in the Manipur Ophiolite Complex, Indo-Myanmar Orogenic Belt, northeast India: Implication for heterogeneous mantle source at the spreading zone. Journal of Asian Earth Sciences, 116:42–58, https://doi.org/10.1016/j.jseaes.2015.11.007

Kieffer B., Arndt, N., Lapierre H., Bastien F., Bosch D., Pecher A., Yirgu

G., Ayalew D., Weis D., Jerram D. A., Keller F., Meugniot, C., 2004. Flood and shield basalts from Ethiopia: Magmas from the African super swell. Journal of Petrology, 45(4):793–834, https://doi.org/10.1093/petrology/egg112

Koptev A., Burov E., Gerya T., Le Pourhiet L., Leroy S., Calais E., Jolivet L., 2018. Plume-induced continental rifting and break-up in ultra-slow extension context: Insights from 3D numerical modeling. Tectonophysics, 746: 121–137, https://doi.org/10.1016/j.tecto.2017.03.025

Koptev, A., Burov, E., Calais, E., Leroy, S., Gerya, T., Guillou-Frottier, L., Cloetingh, S., 2016. Contrasted continental rifting via plume-craton interaction: applications to Central East African rift. Geoscience Frontiers, 7:221–236.

Krans S.R., Rooney T.O., Kappelman J.W., Yirgu G., Ayalew D., 2024. Magma evolution during main-phase continental flood basalt volcanism: A case for recharge-evacuation-assimilation-fractional crystallization in the Ethiopian low-Ti province. Geochemistry, Geophysics, Geosystems, 25:1-36, doi: 10.1029/2023GC011289

Lamotte D.F., Fourdan B., LOeleu S., Leparmentier F., Clarens P., 2015. Style of rifting and the stages of Pangea breakup. AGU Tectonics, 1009-1029, doi: 10.1002/2014TC003760.

Le Gall N. & Pichavant M., 2016. Homogeneous bubble nucleation in H2O- and H2O-CO2-bearing basaltic melts: Results of high temperature decompression experiments. Journal of Volcanology and Geothermal Research, 327:604–62, http://dx.doi.org/10.1016/j.jvolgeores.2016.10.004

Le Maitre, R.W., Bateman, P., Dudek, A., Keller, J., Lemeyre, J., Le Bassabine, P.A., Schimid, R., Sorensen, H., Streckeisen, A., Wooley, A.R., Zanettin, B., 1989. A Classification of Igneous Rocks and Glossary of Terms. Blackwell, Oxford, p. 193

Lebedev S., Meier T., Van der Hilst R. D., 2006. Asthenospheric flow and origin of volcanism in the Baikal Rift area. Earth and Planetary Science Letters, 249(3–4):415–424. https://doi.org/10.1016/j.epsl.2006.07.007

Leterrier J., Maury R.C., Thonon P., Girard D., Marchal M., 1982. Clinopyroxene composition as a method of identification of the magmatic affinities of paleovolcanic series. Earth and Planetary Science Letters, 59(1):139–154, https://doi.org/10.1016/ 0012-821X(82)90122-4.

Liu H., Li Y., Wu L., Huangfu P., Zhang M., 2018. Geochemistry of high-Nb basalt-andesite in the Erguna Massif (NE China) and implications for the early Cretaceous back-arc extension. Geological Journal, 54:291–307, doi: 10.1002/gj.3176

Loparev A., Rouby D., Chardon D., Dall'Asta M., Sapin F., Baby P., Ballard F., Ye J., Paquet F., 2021. Superimposed Rifting at the Junction of the Central and Equatorial Atlantic: Formation of the Passive Margin of the Guiana Shield. Tectonics, 40, https://doi.org/10.1029/2020TC006159

Mader H.M., Llewellin E.W., Mueller S.P., 2013. The rheology of two-phase magmas: A review and analysis. Journal of Volcanology and Geothermal Research, 257:135–158, http://dx.doi.org/10.1016/j.jvolgeores.2013.02.014

Mangan M.T., Cashman K.V., Newman S., 1993. Vesiculation of basaltic magma during eruption. Geology, 21 (2): 157–160.

Maniar, P.D. & Piccoli, P.M., 1989. Tectonic discrimination of granitoids. Geological Society of American Bulletin, 101:635–643.

Marzoli A., Callegaro S., Corso J.D., Davies J.H.F.L., Chiaradia M., Youbi N., Bertrand H., Reisberg L., Merle R., Jourdan F., 2018. The Central Atlantic Magmatic Province (CAMP): A Review. In: Tanner, L. (eds) The late Triassic world: earth in a time of transition. Topics in Geobiology, vol 46. Springer, https://doi.org/10.1007/978-3-319-68009-5_4

Marzoli A., Renne P. R., Piccirillo E. M., Ernesto M., Bellieni G., De Min, A., 1999. Extensive 200-million-year-old continental flood basalts of the Central Atlantic Magmatic Province. Science. www.sciencemag.org

Matos R.D., 2000. Tectonic evolution of the Equatorial South Atlantic. Geophysical Monograph Series, 115:331- 353, doi: 10.1029/GM115p0331

May P.R., 1971. Pattern of Triassic-Jurassic diabase dykes around the North Atlantic in the context of pre-rift position in continents. GSA Bulletin, 82:1285-1291.

McHone J. G., 2000. Non-plume magmatism and rifting during the opening of the central Atlantic Ocean. Tectonophysics, 316:287-296.

McKenzie D., Bickle M.J., 1988. The Volume and Composition of Melt Generated by Extension of the Lithosphere, Journal of Petrology, 29(3):625–679, https://doi.org/10.1093/petrology/29.3.625

McMillan K., Long P. E., Cross R. W., 1989. Vesiculation in Columbia River Basalts. In: Volcanism and tectonism in the Columbia River flood-basalt province, S. P. Reidel and P. R. Hooper (editor)
Special Paper - Geological Society of America, 239: 157-167.

Menezes F., Wankler F., Veloso R., Gama C.C., 2020. Sistemas deposicionais fluviais: análise estratigráfica das unidades sedimentares da Formação Boa Vista, nordeste da bacia do Tacutu, RR. Revista Geográfica Acadêmica, 14(1):69–93.

Merle R., Marzoli A., Reisberg L., Bertrand H., Nemchin A., Chiaradia M., Callegaro S., Jourdan F., Bellieni G., Kontak D., Puffer J., McHone J.G., 2014. Sr, Nd, Pb and Os isotope systematics of CAMP tholeiites from Eastern North America (ENA): evidence of a subduction-enriched mantle source. Journal of Petrology, 55(1):133-180, doi:10.1093/petrology/egt063

Milani E.J. & Thomaz Filho A. 2000. Sedimentary Basins of South America. In: Cordani, U.G., Milani, E.J., Thomaz Filho, A. Campos, D.A. (Eds.), Tectonic Evolution of South America. Rio de Janeiro, 31st, SBG/IGC, 389-449.

Mohriak W.U., 2003. Bacias Sedimentares da Margem Continental Brasileira. In: L.A. Bizzi, C. Schobbenhaus, R.M. Vidotti e J.H. Gonçalves (eds.). Geologia, Tectônica e Recursos Minerais do Brasil, CPRM, Brasília, c. III, p. 87-165.

Morimoto, N., 1988. Nomenclature of pyroxenes. Mineralogy and Petrology, 39:55–76, https://doi. org/10.1007/BF01226262.

Nebel O., Scherer E.E., Mezger K., 2011. Evaluation of the 87Rb decay constant by age comparison against the U–Pb system. Earth and Planetary Science Letters, 301(1-2):1-8, https://doi.org/10.1016/j.epsl.2010.11.004

Niu Y., 2021. Lithosphere thickness controls the extent of mantle melting, depth of melt extraction and basalt compositions in all tectonic settings on Earth – A review and new perspectives. Earth-Science Reviews 217:103614, https://doi.org/10.1016/j.earscirev.2021.103614

Oliveira A.L., Schmitz M.D., Wall C.J., Hollanda M.H.B.M., 2022. A bulk annealing and dissolution-based zircon concentration method for mafic rocks. Chemical Geology, 597:120817, https://doi.org/10.1016/j.chemgeo.2022.120817

Passos M. S. & Vidotti R., 2019. Análise e interpretação do arcabouço tectônico do rifte do Tacutu, Roraima, Brasil - com base em dados magnéticos. In: Boletim de Resumos Expandidos do XVI Simpósio de Geologia da Amazônia, SBG-NO, Manaus, CD-ROM.

Peace A.L., Phethean J.J.J., Franke D., Foulger G.R., Schiffer C., Welford J.K., McHone G., Rocchi S., Schnabel M., Doré A.G., 2020. A review of Pangaea dispersal and Large Igneous Provinces – In search of a causative mechanism. Earth-Science Reviews, 206:102902, doi: 10.1016/j.earscirev.2019.102902.

Pearce J.A. & Norry M.J., 1979. Petrogenetic implications of Ti, Zr, Y, and Nb variations in volcanic rocks. Contribution to Mineralogy and Petrology, 69:33-47.

Pérez-Gussinye M., 2013. A tectonic model for hyperextension at magma-poor rifted margins: an example from the West Iberia–Newfoundland conjugate margins. In: Mohriak, W. U., Danforth, A., Post, P. J., Brown, D. E., Tari, G. C., Nemcok, M., Sinha, S. T. (eds). Conjugate Divergent Margins. Geological Society, London, Special Publications, 369, 403–427.

Petersen M.D., 1983. The use of the "immobile" elements Zr and Ti in lithogeochemical exploration for massive sulphide deposits in the Precambrian Pecos greenstone belt of northern New Mexico. Journal of Geochemical Exploration, 19, 615-617.

Pfänder J. A., Jung S., Münker C., Stracke A., Mezger K., 2012. A possible high Nb/Ta reservoir in the continental lithospheric mantle and consequences on the global Nb budget: evidence from continental basalts from Central Germany. Geochimica et Cosmochimica Acta, 77:232–251. https://doi.org/10.1016/j.gca.2011.11.017

Pinto V.M., Santos J.O.S., Ronchi L. H., Hartmann L.A., Bicudo C.A., Souza V., 2017. Field and geochemical constraints on the relationship between the Apoteri basalts (northern Brazil, southwestern Guyana) and the Central Atlantic Magmatic Province. Journal of South American Earth Sciences, 79: 384–393, https://doi.org/10.1016/j.jsames.2017.08.015

Pinto V.M., Santos J.O.S., Ronchi L.H., Koester E., Hartmann L.A., Souza V., Schneider B.C., Mayer D. E., 2020. Sr-Nd-Pb geochemical constraints on the relationship between Apoteri basalts (northern Brazil and Guyana) and the Central Atlantic Magmatic Province. In: Anais do 48o Congresso Brasileiro de Geologia, SBG, Porto Alegre, resumos, CD-ROM.

Pirajno F., & Santosh M., 2015. Mantle plumes, supercontinents,

intracontinental rifting and mineral systems. Precambrian Research, 259:243–261. https://doi.org/10.1016/j.precamres.2014.12.016

Polacci M., Baker D.R., La Rue A., Mancini L., Allard P., 2012. Degassing behaviour of vesiculated basaltic magmas: an example from Ambrym volcano, Vanuatu Arc. Journal of Volcanology and Geothermal Research, 233–234:55–64, doi:10.1016/j.jvolgeores.2012.04.019

Reis N.J., Nunes N.S.V., Pinheiro S.S.S., 1994. A cobertura mesozoica do hemigráben Tacutu – Estado de Roraima: uma abordagem ao paleoambiente da Formação Serra do Tucano. Anais do 38º Congresso Brasileiro de Geologia, Balneário Camboriú (SC), v.3, p.234-235.

Reis N.J., Faria M.S.G., Maia, M.A.M., 2001. O quadro Cenozóico da porção norte-oriental do Estado de Roraima. In: E.L. Klein, M.L. Vasquez, L.T. da Rosa-Costa (Eds.), Contribuição à Geologia da Amazônia, SBG-NO, Belém, v.3, p. 259-272.

Reis N.J., Fraga L.M., Faria M.S.G., Almeida M.E., 2003. Geologia do Estado de Roraima, Brasil. Géologie de La France, 4:121–134.

Reis N.J., Szatmari P., Filho J.R.W., York D., Evensen N.M., Smith P.E., 2006. Dois eventos de magmatismo máfico mesozóico na fronteira Brasil-Guiana, escudo das Guianas enfoque à região do rifte Tacutu-North Savannas. In: Anais do XLIII Congresso Brasileiro de Geologia, SBG, Aracajú, CD-ROM.

Reis N.J., Teixeira W., Hamilton M.A., Bispo-Santos F., Almeida M.E., D'Agrella-Filho M.S., 2013. Avanavero mafic magmatism, a late Paleoproterozoic LIP in the Guiana Shield, Amazonian Craton: U-Pb ID-TIMS baddeleyite, geochemical and paleomagnetic evidence. Lithos, 174:175–195. https://doi.org/10.1016/j.lithos.2012.10.014

Rivalta E., Pascal K., Phillips J., Bonaccorso A., 2013. Explosive expansion of a slowly decompressed magma analogue: evidence for delayed bubble nucleation. Geochemistry, Geophysics, Geosystems, 14:3067–3084, doi:10.1002/ggge.20183.

Rollinson H., 1993. Using Geochemical Data: Evaluation, Presentation, Interpretation. Longman Scientific & Technical, Singapore, p. 352p.

Rosenbaum G., Weinberg R.F., Regenauer-Lieb K., 2008. The geodynamics of lithospheric extension. Tectonophysics, 458:1-8, doi:10.1016/j.tecto.2008.07.016.

Ruppel C., 1995. Extensional processes in continental lithosphere. JGR Solid Earth, 100(B12): 24187-24215, https://doi.org/10.1029/95JB02955

Saar M.O. & Manga M., 1999. Permeability-porosity relationship in vesicular basalts. Geophysical Research Letters, 26(1):111-114.

Sahagian D. & Proussevitch A., 2007. Paleoelevation measurement on the basis of vesicular basalts. Reviews in Mineralogy and Geochemistry, 66(1):195–213. doi: https://doi.org/10.2138/rmg.2007.66.8

Sahagian D. L., Proussevitch A. A., Carlson W.D., 2002. Analysis of vesicular basalts and lava emplacement processes for application as a paleobarometer/paleoaltimeter. The Journal of Geology, 110:671-685, https://doi.org/10.1086/342627

Santos J.O.S., Hartmann L.A., Gaudette H.E., Groves D.I., Mcnaughton N.J., Fletcher I.R.A., 2000. A new understanding of the provinces of the Amazon craton based on integration of field mapping and U-Pb and Sm-Nd geochronology. Gondwana Research, 3(4):453-488.

Santos, J.O.S. dos, Reis, N.J., Chemale F., Hartmann, L.A., Pinheiro, S.da.S., McNaughton, N.J., 2003. Paleoproterozoic evolution of Northwestern Roraima State-absence of archean crust, based on U-Pb and Sm-Nd isotopic evidence. In: Simposyum of South-American on Isotope Geology, vol. 4, Pucon, Chile, CD-ROM.

Saunders A.D. & Tarney J., 1984. Geochemical characteristics of basaltic volcanism within back-arc basins. In: B.P. Kokelaar & M.F. Howells (Eds.), Marginal basin geology, Geological Society of London, special publication, 16:59-76.

Sengör A.M.C. & Burke K., 1978. Relative timing of rifting and volcanism on Earth and its tectonic implications. Geophysical Research Letters, 5(6): 419-421, https://doi.org/10.1029/GL005i006p00419

Silva A.J.P., Lopes R.C., Vasconcelos A.M., Bahia R.B.B., 2003. Bacias Sedimentares Paleozóicas e Meso-Cenozóicas Interiores. In: L. A. Bizzi, C. Schobbenhaus, R. M. Vidotti e J. H. Gonçalves (eds.), Geologia, Tectônica e Recursos Minerais do Brasil, CPRM, Brasília, c.II, p.55-85.

Simon K., Huismans R.S., Beaumont C., 2009. Dynamical modelling of lithospheric extension and small-scale convection: implications for magmatism during the formation of volcanic rifted margins. Geophysical Journal International, 176:327–350, doi: 10.1111/j.1365-246X.2008.03891.x

Smets B., Delvaux D., Ross K. A., Poppe S., Kervyn M., D'Oreye N., Kervyn F., 2016. The role of inherited crustal structures and magmatism in the development of rift segments: Insights from the Kivu basin, western branch of the East African Rift. Tectonophysics, 683:62–76, https://doi.org/10.1016/j.tecto.2016.06.022

Soldati A., Ferrell J.A., Sant C., Wysocki R., Karson J.A., 2020. The effect of bubbles on the rheology of basaltic lava flows: Insights from large-scale two-phase experiments. Earth and Planetary Science Letters 548:116504, https://doi.org/10.1016/j.epsl.2020.116504

Stab, M., N. Bellahsen, R. Pik, X. Quidelleur, Ayalew D., Leroy S., 2016. Modes of rifting in magma-rich settings: Tectono-magmatic evolution of Central Afar. Tectonics, 35:2-38, doi:10.1002/ 2015TC003893.

Sun S.S., 1980. Lead isotopic study of young volcanic rocks from mid-ocean ridges, ocean islands and island arcs. Philosophical Transactions of the Royal Society, A297:409-445.

Tang, M., Lee, C. T. A., Chen, K., Erdman, M., Costin, G., & Jiang, H., 2019. Nb/Ta systematics in arc magma differentiation and the role of arclogites in continent formation. Nature Communications, 10:235, https://doi.org/10.1038/s41467-018-08198-2.

Tassinari C.C.G. & Macambira M.J.B., 1999. Geochronological provinces of the Amazonian Craton. Episodes, 22:174-182.

Theunissen T. & Huismans R.S., 2022. Mantle exhumation at magma-poor rifted margins controlled by frictional shear zones. Nature Communications, https://doi.org/10.1038/s41467-022-29058-1

Thirlwall M.F., 1991. High-precision multicollector isotopic analysis of low levels of Nd as oxide. Chemical Geology, 94(1):13-22, https://doi.org/10.1016/S0009-2541(10)80013-0

Thomaz Filho A., Mizusaki A.M.P., Milani E.J., Cesero P., 2000. Rifting and magmatism associated with the South America and Africa break up. Revista Brasileira de Geociências, 30(1):17-19.

Vaz P.T., Wanderley Filho J.R., Bueno G.V., 2007. Bacia do Tacutu. Boletim de Geociências da Petrobras, Rio de Janeiro, 15(2):289-297.

Verati C., Bertrand H., Féraud G., 2005. The farthest record of the Central Atlantic Magmatic Province into West Africa craton: Precise 40Ar/39Ar dating and geochemistry of Taoudenni basin intrusives (northern Mali). Earth and Planetary Science Letters, 235:391-407, doi:10.1016/j.epsl.2005.04.012

Vermeesch P. & Pease V., 2021. A genetic classification of the tholeiitic and calc-alkaline magma series. Geochemical Perspectives Latters, 19:1-6, doi: 10.7185/geochemlet.2125.

Wang J., Su B. X., Robinson P. T., Xiao Y., Bai Y., Liu X., Sakyi P. A., Jing J. J., Chen C., Liang Z., Bao Z.A., 2021. Trace elements in olivine: Proxies for petrogenesis, mineralization and discrimination of mafic-ultramafic rocks. Lithos, 388–389:106085, doi:10.1016/j.lithos.2021.106085.

Wang Z-Z. and Liu S-A., 2021. Evolution of intra-plate alkaline to tholeiitic basalts via interaction between carbonated melt and lithospheric mantle. Journal of Petrology, 1-25, doi: 10.1093/petrology/egab025

Webster R.E., Nibbelink K., Boyce D., 2020. Takutu Basin Rift as a Late Cretaceous Conduit for Continent-Interior Drainage into the Guyana Basin. Adapted from oral presentation accepted for the 2020 AAPG, Annual Convention and Exhibition online meeting, article #30679, doi:10.1306/30679Webster2022.

White R. & McKenzie D., 1989. Magmatism at rift zones: the generation of volcanic continental margins and flood basalts. JGR Solid Earth, 94(B6):7685-7729, https://doi.org/10.1029/JB094iB06p07685

Whitmarsh, R., Manatschal, G., Minshull, T. 2001. Evolution of magma-poor continental margins from rifting to seafloor spreading. Nature, 413:150–154. https://doi.org/10.1038/35093085

Wilson M., 1995. Igneous petrogenesis: a global tectonic approach. Chapman & Hall, New York, 466p.

Wilson L.J.E., Giacalone E., Scott J.M., Brenna M., White J.D.L., Roux P.J., Hemming S.R., Palmer M. C., Read S.E., Reid M.R., Stirling C.H., 2025. Contemporaneous alkaline and subalkaline intraplate magmatism in the Dunedin Volcanic Group, NZ, caused by mantle heterogeneity. New Zealand Journal of Geology and Geophysics, 68(1):95-119 doi:10.1080/00288306.2023.2277443.

Winchester J.A. & Floyd P.A., 1977. Geochemical discrimination of different magma series and their differentiation products using immobile elements. Chemical Geology, 20:325-343.

Windley B.F., 1995. The evolving continents. John Wiley & Sons Ltd, New York, 526p.

Xia L-Q., 2014. The geochemical criteria to distinguish continental basalts from arc related ones. Earth-Science Reviews, 139:195-212, doi: 10.1016/j.earscirev.2014.09.006.

Xia, L., Xia, Z., Xu, X., Li, X., Ma, Z., 2013. Late Paleoproterozoic rift-related magmatic rocks in the North China Craton: geological records

of rifting in the Columbia supercontinent. Earth Science Reviews, 125: 69–86. https://doi.org/10.1016/j. earscirev.2013.06.004.

Ye J., Chardon D., Rouby D., Guillocheau F., Dall'asta M., Ferry J-N., Broucke O., 2017. Paleogeographic and structural evolution of northwestern Africa and its Atlantic margins since the early Mesozoic. Geosphere, 13(4):1254-1284, doi:10.1130/GES01426.1.

Zhang Y., Yu K., Qian H., 2018. LA-ICP-MS analysis of clinopyroxenes in basaltic pyroclastic rocks from the Xisha islands, northwestern south China sea. Minerals, 8: 575. https://doi.org/10.3390/min8120575.

Zhao Y-W., Zou H., Li N., Wei W., Yuan C., Fan Q-C., X-B. Zhang, 2020. Petrogenesis of late Cenozoic basalts from Dalinor, Inner Mongolia: Implications for lateral mantle heterogeneity in eastern China. Lithos, 366–367. https://doi.org/10.1016/j.lithos.2020.105561.

Zhao Z., Sun S.Q., Liu Z.Q., Ma H.S., Xiang B., Zhao S.J., 2021. Th, Nb and Zr characteristics and plume causes identification of Emeishan basalts. 11th Conference of Asian Rock Mechanics Society, IOP Conference Series: Earth and Environmental Science, 861:052086, https://doi.org/10.1088/1755-1315/861/5/052086.

Zwaan F., Schreurs G., Adam, J., 2018. Effects of sedimentation on rift segment evolution and rift interaction in orthogonal and oblique extensional settings: Insights from analogue models analyzed with 4D X-ray computed tomography and digital volume correlation techniques. Global and Planetary Change, 171:110–133, https://doi.org/10.1016/j.gloplacha.2017.11.002.

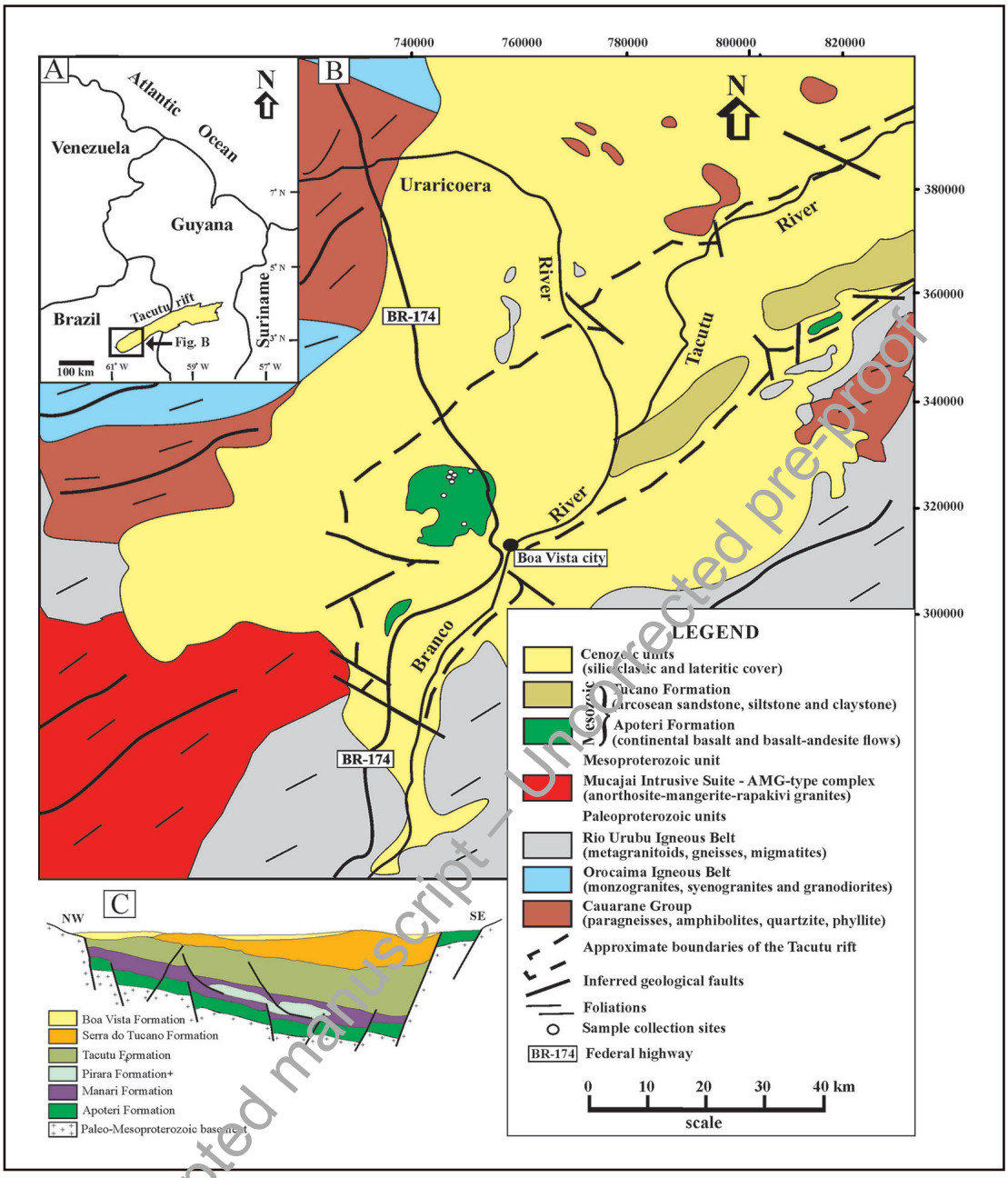

Figure 1: A) Geographic location of the Tacutu continental rift on the border of Brazil and Guyana; B) Simplified regional geological map of the Mesozoic Tacutu Basin area on the Brazil side, indicating the sampling site of the Apoteri basaltic rocks (Modified from CPRM 2022); C) Simplified and schematic geological section of the Tacutu hemi-graben basin (adapted and modified from Reis et al. 1994)

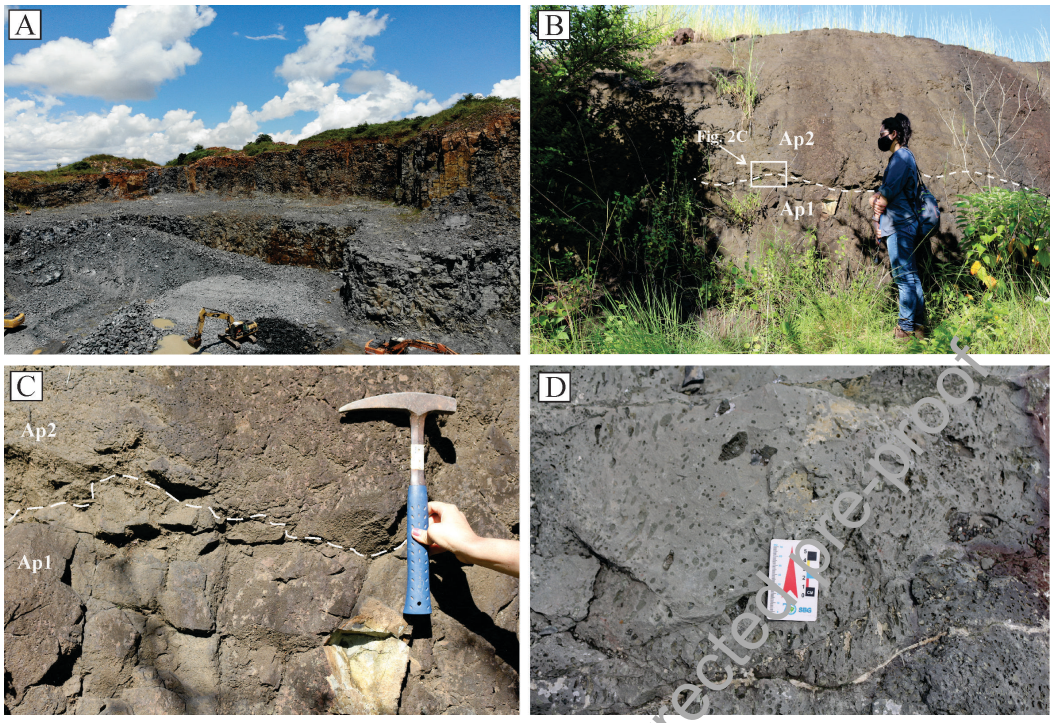

Figure 2: Outcrops of the Apoteri basaltic rocks. A) Open pit mine for crushed basalt stone of the Granada Company; B) Field relationship between the two Apoteri basaltic lava flows; C) Geological contact detail between the two Apoteri basaltic lava flows; C) Vesicular enrichment and coalescence zone in the Ap2 basaltic lava flow.

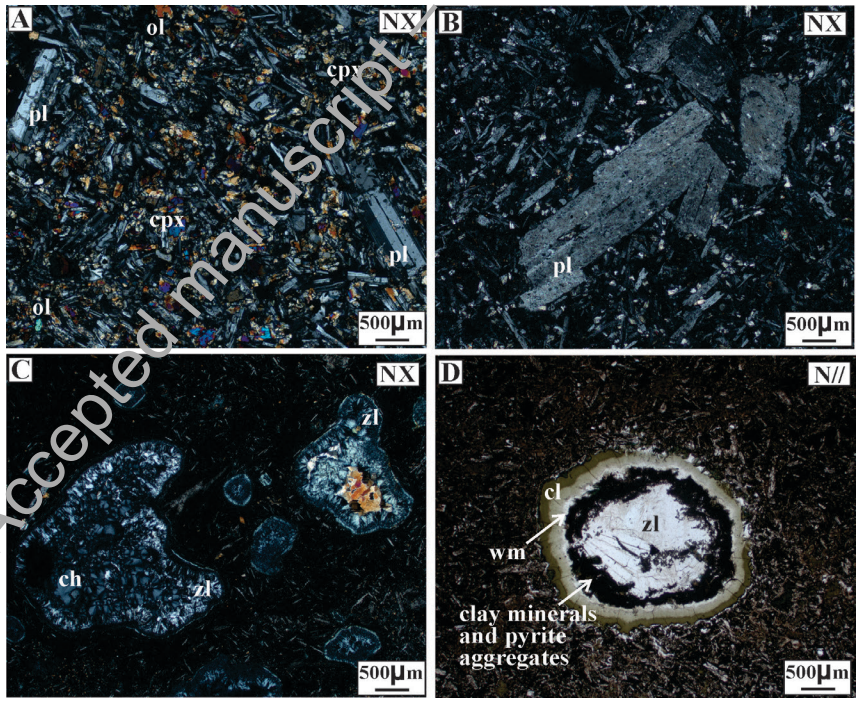

Figure 3: Petrographic features of the Apoteri basaltic rocks. A) Ophitic to sub-ophitic common micro-texture marked by plagioclase phenocrysts embedded in fine-grained groundmass with interstitial clinopyroxene and olivine (Ap1 sample); B) Plagioclase phenocrysts in glomeroporphyritic micro-texture embedded in fine-grained groundmass (Ap1 sample); C) Vesicles embedded in an ophitic to sub-ophitic micro-texture. Note the size variation of the vesicles, which may indicate some degree of coalescence of the volatile phase (Ap2 sample); D) Detail of the internal mineral zonation of the vesicles in Ap2 sample (pl = plagioclase, cpx = clinopyroxene, ol = olivine, ch = chalcedony, cl = chlorite, zl = zeolite, wm = white mica, NX = crossed nicols, N// = parallel nicols).

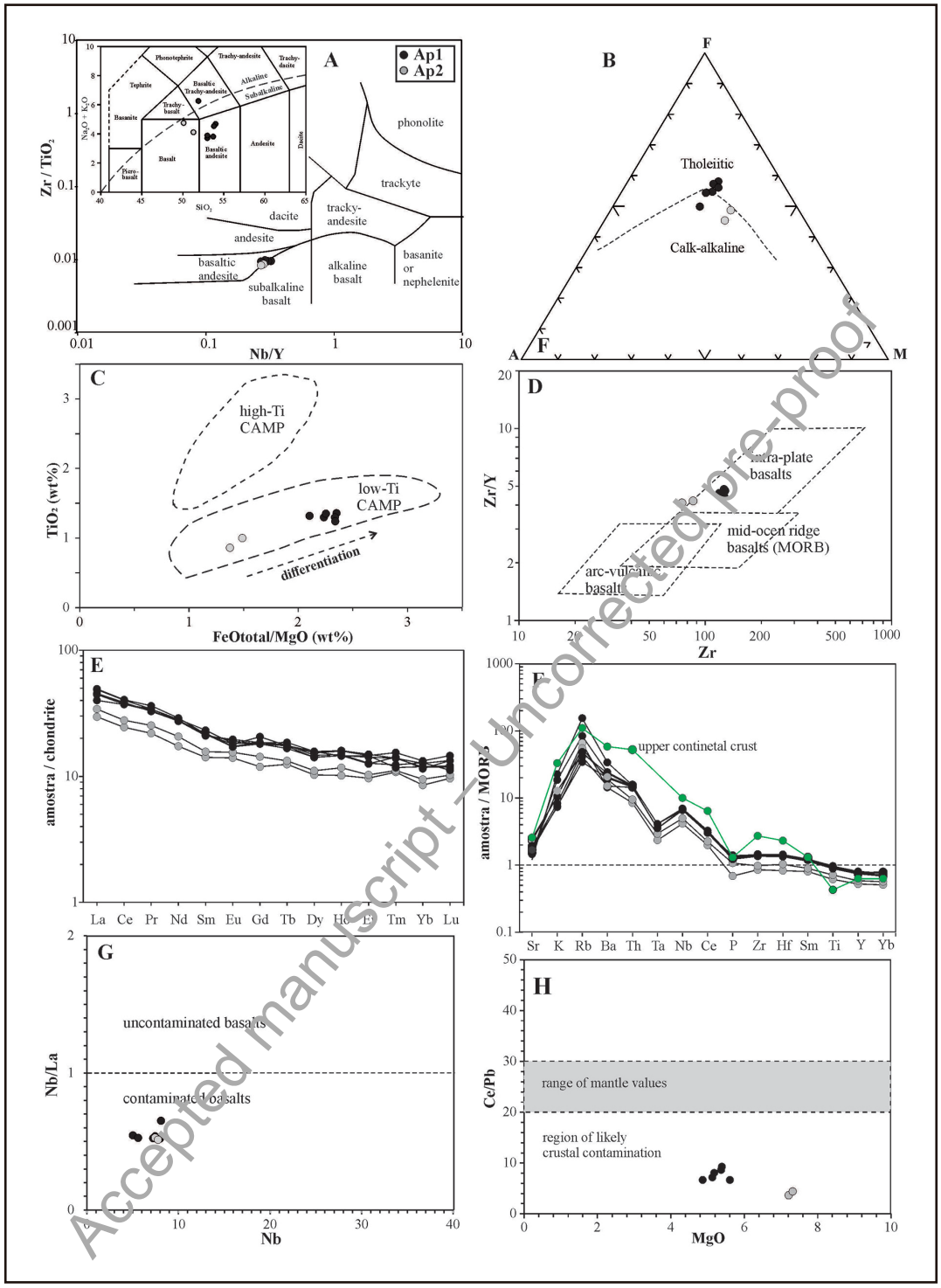

Figure 4: Geochemical characteristics of the Ap1 and Ap2 basaltic rocks from the Apoteri Formation. A) Na2O + K2O x SiO2 and Zr/TiO2 x Nb/Y for volcanic rocks discriminant diagrams (Le Maitre et. al 1989 and Winchester & Floyd 1977); B) AFM discriminant diagram for tholeiitic and calc-alkaline fields (Irvine & Baragar 1971); C) TiO2 x FeOtot/MgO diagram indicating the CAMP-type continental flood basalts fields (Chabou et al. 2010); D) Zr/Y x Zr tectonic fields diagram (Pearce and Norry 1979); E) REEs-normalized pattern diagram (chondrite-normalized pattern of Boynton 1984); F) Multi-element spidergram pattern diagram. Note the comparison with the distribution pattern of the continental crust (MORB-normalized pattern of Saunders & Tarney 1984 with additions from Sun 1980); G-H) Nb/La x Nb and Ce/Pb x MgO discriminant diagrams applied to crustal contamination rates (Xia 2014; Furman 2007). Note the variation in MgO content leading to the formation of two groups of samples.

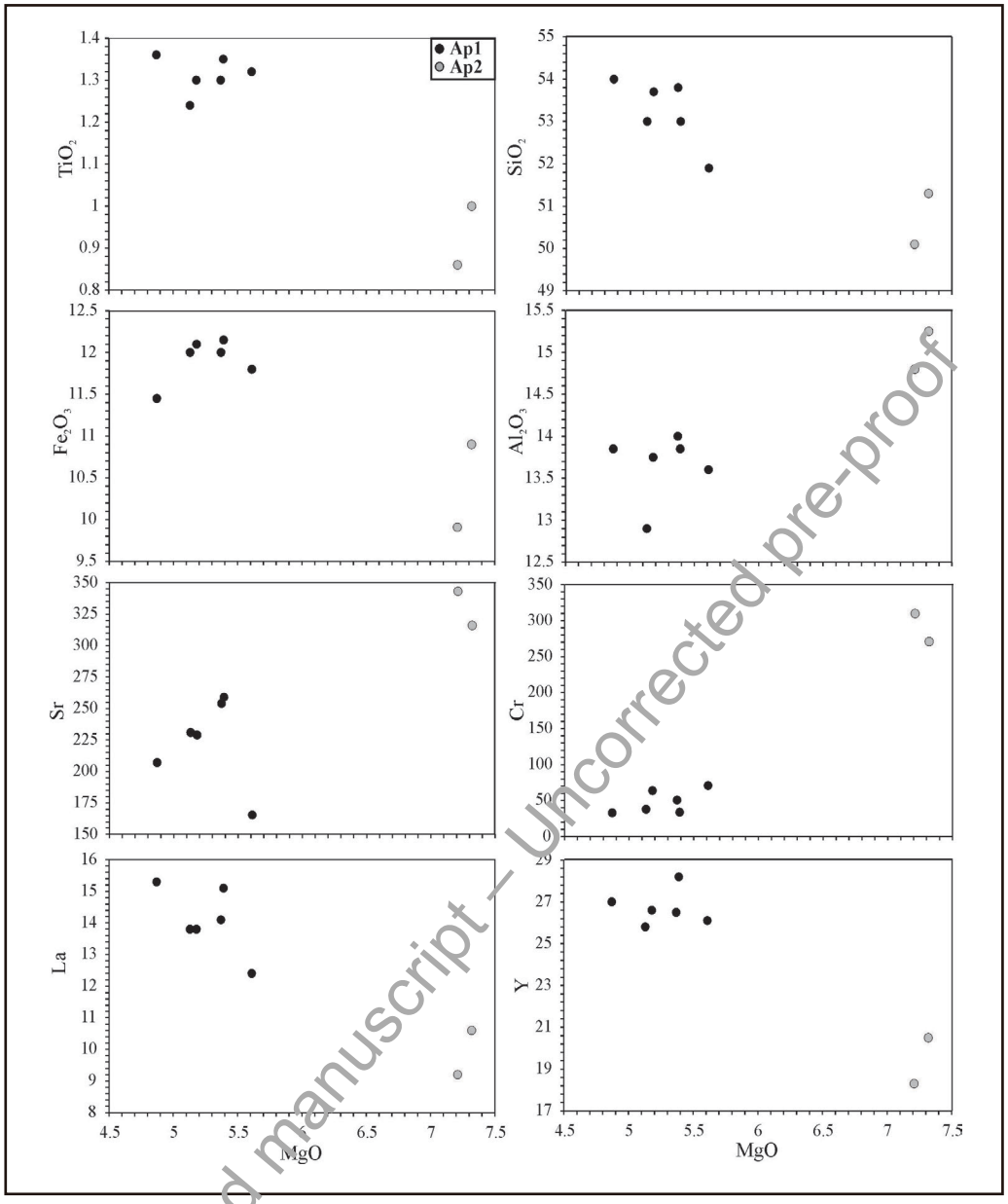

Figure 5: Fenner-type element variation diagrams of the Ap1 and Ap2 basaltic rocks from the Apoteri Formation. Selected major and trace elements versus MgO

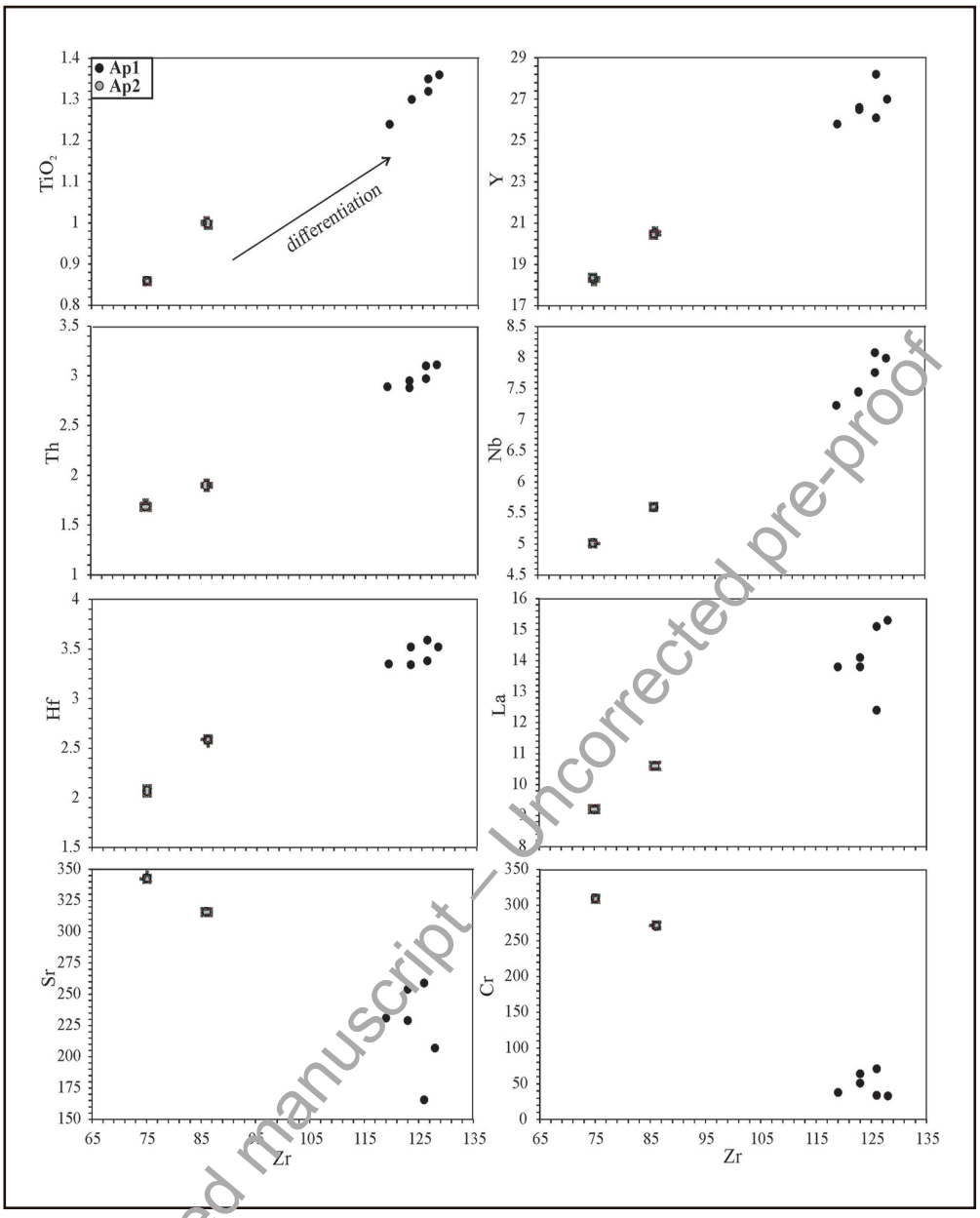

Figure 6: Zr versus selected major and trace elements diagrams applied for possible evaluation of the geochemical mobility of elements in the Ap1 and Ap2 basaltic rocks from the Apoteri Formation.

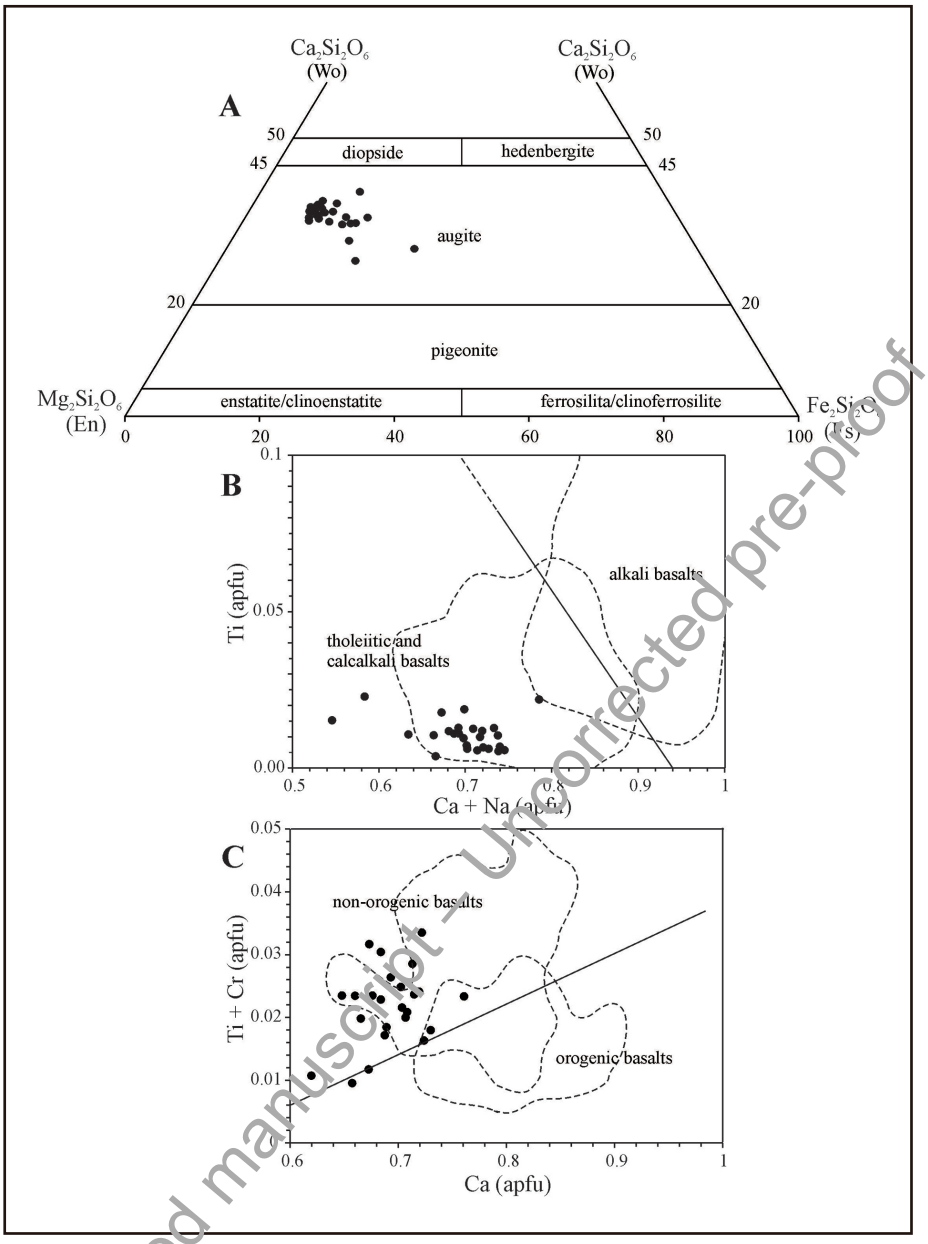

Figure 7: Pyroxene mineral chemistry diagrams applied to the Apoteri basaltic rocks. A) Mineral chemistry plot on Ca–Mg–Fe pyroxenes in the Fs-Wo-En ternary diagram (after Morimoto et al., 1988); B and C) Tectonic discriminant diagrams based on mineral chemistry. Note that analyzed spots plot on the tholeiitic and non-orogenic basalts fields, respectively (adapted from Leterrier et al., 1982).

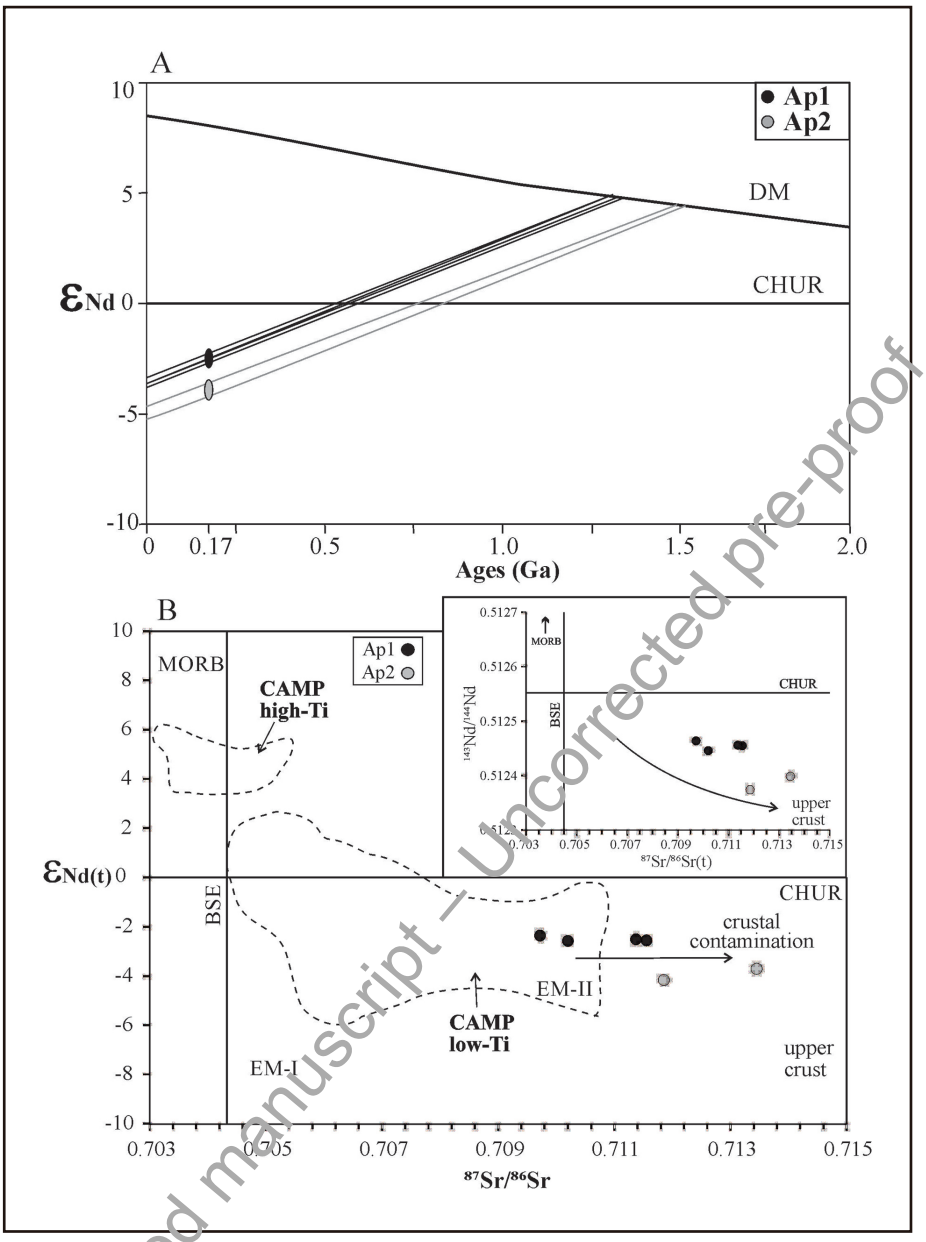

Figure 8: Nd and Sr isotope ratios characteristics of basaltic rocks of the Apoteri Formation. A) ƐNd x Age (Ga) evolution patterns diagram applied to basaltic rocks of the Apoteri Formation. Depleted mantle (DM) curve according to DePaolo (1981); B) 143Nd/144Nd x 87Sr/86Sr and ƐNd x 87Sr/86Sr associated diagrams with time (t) back-calculated to 175 Ma, indicating the important role of mantle-crust interaction/ contamination rate and the isotopic correspondence with low-Ti CAMP basalts. The CAMP field with Nd and Sr isotopes ratios back-calculated to 200 Ma, according to Deckart et al. (2005).

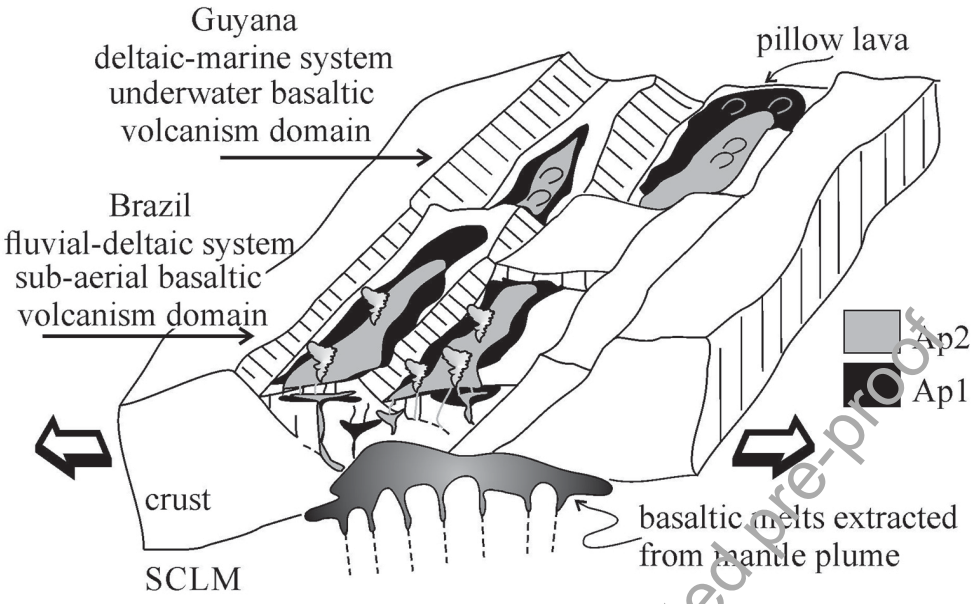

Figure 9: A simplified geological model proposed for the emplacement moments of the Apoteri Ap1 (A) and Ap2 (B) basaltic lava flows during the Tacutu pre-rift phase (early Jurassic). The Tacutu rift internal geometry favored sub-aerial fissure basaltic volcanism with some degree of explosivity in the Ap2 pulse, associated with a fluvial-deltaic system on the Brazilian side, as well as underwater fissure volcanism associated with deltaic-marine systems on the Guyana side.

Table 1: Whole-rock geochemistry of the Ap1 and Ap2 basaltic rocks from the Apoteri Formation.

Lava flow	AP1						AP2	
Samples	SO-02	SO-23	SO-26	SO-27	SO-28	SO-29	SO-04	SO-20
SiO2 (%)	54.00	51.90	53.70	53.00	53.80	53.00	50.10	51.30
Al2O3	13.85	13.60	13.75	12.90	14.00	13.85	14.80	15.25
TiO2	1.36	1.32	1.30	1.24	1.30	1.35	0.86	1.00
Fe2O3	11.45	11.80	12.10	12.00	12.00	12.15	9.91	10.90
CaO	8.18	6.75	8.72	8.69	8.16	8.69	8.15	9.68
MgO	4.87	5.61	5.18	5.13	5.37	5.39	7.21	7.32
Na2O	2.84	3.31	2.54	2.96	3.81	3.06	3.72	3.06
K2O	1.85	2.96	1.28	0.75	0.73	0.83	1.04	1.06
MnO	0.18	0.19	0.18	0.17	0.19	0.2	0.17	0.18
P2O5	0.16	0.18	0.18	0.16	0.17	0.17	0.09	0.14
LOI	1.68	2.00	0.83	1.51	1.65	1.31	2.35	1.51
Total	100.48	99.7	99.83	98.56	101.24	100.57	98.5	101.5
Ba (ppm)	291.00	406.00	282.00	237.00	181.01	248	172.01	227.00
Rb	83.91	154.00	46.40	34.32	41.40	48.62	65.40	55.20
Sr	207.00	165.50	229.00	231.01	254.01	259.00	343.00	316.02
Hf	3.52	3.38	3.52	3.35	3.34	3.59	2.07	2.58
Cr	33.02	71.00	64.10	38.03	51.00	34.04	31.10	37.04
Cs	0.84	0.4	0.63	0.56	0.59	0.54	0.81	0.87
Nb	7.99	8.08	7.44	7.23	7.45	7.76	5.02	5.59
Ta	0.71	0.72	0.68	0.66	0.67	0.69	0.44	0.53
Th	3.11	3.12	2.95	2.89	2.88	2.97	1.69	1.92
Sn	2.31	1.82	2.11	2.00	1.94	1.95	1.51	1.40
U	0.81	0.72	0.67	0.72	0.72	0.73	0.46	0.46
V	352.01	340.03	344.02	326.02	346.00	353.01	286.03	300.02
Y	27.00	26.10	26.60	25.80	26.50	28.20	18.31	20.52
Zr	128.00	126.00	123.00	119.00	123.01	126.00	75.02	86.03
Pb	4.93	4.53	3.84	4.20	3.61	3.55	5.46	5.17
La	15.31	12.42	13.80	13.81	14.10	15.10	9.22	10.61
Ce	32.71	30.01	30.72	30.20	31.10	32.50	19.82	22.51
Pr	4.42	4.18	4.06	4.04	3.99	4.17	2.68	3.09
Nd	17.40	16.60	16.41	16.41	16.52	17.00	10.44	12.43
Sm	4.22	4.28	4.15	4.21	4.09	4.52	2.76	3.06
Eu	1.32	1.27	1.40	1.26	1.44	1.34	1.03	1.14
Gd	5.34	4.81	4.67	4.69	4.80	4.76	3.09	3.71
Tb	0.83	0.82	0.83	0.79	0.84	0.88	0.59	0.63
Dy	4.93	4.55	5.08	4.57	4.72	5.06	3.31	3.57
Ho	1.14	1.05	1.04	1.05	1.07	1.15	0.73	0.84
Er	3.07	2.64	3.06	2.98	2.67	3.14	2.03	2.16
Tm	0.54	0.46	0.38	0.45	0.40	0.45	0.35	0.36
Yb	2.77	2.40	2.49	2.48	2.68	2.65	1.78	1.98

Continue

Table 1: Whole-rock geochemistry of the Ap1 and Ap2 basaltic rocks from the Apoteri Formation.

Lava flow	AP1						AP2	
Samples	SO-02	SO-23	SO-26	SO-27	SO-28	SO-29	SO-04	SO-20
Lu	0.47	0.43	0.39	0.38	0.36	0.43	0.31	0.33
Na2O+K2O	4.69	6.27	3.82	3.71	4.54	3.89	4.76	4.12
Mg#	45.73	48.51	45.89	45.86	47.00	46.78	59.04	57.09
A/NK	2.07	1.57	2.47	2.27	1.98	2.33	2.04	2.46
LaN + CeN	89.82	77.12	82.51	81.89	83.97	88.93	54.18	62.04
TmN + YbN	28.68	25.68	23.64	25.75	25.16	26.56	19.31	20.58
LaN/SmN	2.28	1.82	2.09	2.06	2.16	2.10	2.09	2.17
GdN/YbN	1.55	1.61	1.51	1.52	1.44	1.44	1.40	1.51
Eu/Eu*	0.27	0.27	0.31	0.28	0.32	0.28	0.35	0.33
Nb/La	0.52	0.65	0.53	0.52	0.52	0.51	0.54	0.52
La/Nb	1.91	1.53	1.85	1.90	1.89	1.94	1.83	1.89
La/Ba	0.05	0.03	0.04	0.05	0.07	0.06	0.05	0.04
Ce/Pb	6.67	6.66	8.07	7.19	8.63	9.28	3.66	4.41

Table 2: Electron microprobe analysis and representative structural formula of clinopyroxene from Ap1 pulse of the Apoteri Formation.

Spots	1	2	3	4	5	6	7	8	9	10	11	12	13	14	15	16	17	18	19	20	21	22	23	24	25	26
SiO_2	53.54	53.69	53.98	53.82	53.64	53.23	53.35	50.99	50.83	53.05	53.80	53.23	53.53	53.46	53.25	53.66	53.14	53.16	53.08	52.99	53.10	53.01	51.67	52.62	51.99	52.84
TiO_2	0.26	0.222	0.24	0.466	0.206	0.375	0.196	0.375	0.427	0.452	0.461	0.358	0.136	0.63	0.349	0.402	0.434	0.207	0.226	0.25	0.547	0.675	0.798	0.778	0.394	0.385
Al_2O_3	2.031	2.05	2.034	2.191	2.266	2.179	2.412	4.361	4.403	2.654	2.154	1.87	1.782	2.024	2.477	2.44	2.54	2.50	2.84	2.788	1.615	1.718	1.869	2.04	1.972	1.409
FeO	6.688	6.475	6.422	6.668	6.167	6.427	6.309	9.781	7.899	6.859	7.499	7.856	9.238	10.83	5.902	5.911	5.745	5.722	5.674	5.879	12.514	9.317	16.678	8.896	10.541	10.937
MgO	18.357	18.321	18.086	18.371	17.643	17.772	17.851	16.623	17.947	17.66	16.752	17.789	17.386	15.381	19.205	19.161	18.929	19.106	18.863	18.281	17.931	17.079	14.03	15.199	16.872	17.896
CaO	17.461	17.446	17.978	17.214	18.528	18.195	18.36	16.301	16.731	17.523	18.06	17.95	16.508	16.559	17.498	17.278	17.991	18.025	18.35	18.498	13.439	17.269	13.984	18.976	16.859	15.615
Na_2O	0.173	0.208	0.193	0.225	0.216	0.257	0.203	0.216	0.291	0.222	0.256	0.123	0.115	0.098	0.197	0.198	0.244	0.147	0.198	0.258	0.16	0.209	0.173	0.339	0.276	0.202
K_2O	0.019	0.016	0.01	0.017	0.016	0.005	0.006	0.079	0.018	0	0.015	0.018	0	0.047	0.019	0	0.005	0.021	0.014	0	0.005	0	0	0.016	0.005	0.035
MnO	0.117	0.305	0.133	0.209	0.151	0.082	0.126	0.217	0.115	0.169	0.192	0.076	0.226	0.363	0.182	0.194	0.156	0.217	0.081	0.139	0.413	0.209	0.382	0.183	0.227	0.285
P_2O_5	0	0.073	0	0	0.09	0	0.088	0.071	0	0.054	0	0	0	0.04	0	0.006	0.01	0	0.044	0.023	0	0	0.014	0	0.064	0.038
Cr_2O_3	0.386	0.379	0.461	0.367	0.422	0.47	0.375	0.444	0.399	0.474	0.372	0.376	0.195	0.069	0.461	0.719	0.45	0.552	0.78	0.926	0.117	0.399	0.04	0.049	0.024	0
F	0	0	0	0	0.139	0.212	0.136	0.073	0.048	0	0	0	0	0	0.005	0.049	0.163	0	0.212	0	0.188	0	0	0.241	0	0
Cl	0.005	0	0.002	0	0	0.002	0	0	0.013	0.031	0	0.003	0	0.013	0.005	0	0	0.013	0.005	0.022	0.013	0	0	0.008	0.029	0
NiO	0.047	0.126	0	0.079	0.131	0.042	0	0.031	0.004	0.03	0.068	0.011	0	0.077	0	0.037	0.076	0.072	0.098	0.043	0.052	0.039	0	0	0.048	0.015
Total	**99.092**	**99.318**	**99.548**	**99.632**	**99.562**	**99.160**	**99.359**	**99.538**	**99.108**	**99.176**	**99.630**	**99.659**	**99.116**	**99.535**	**99.548**	**100.037**	**99.818**	**99.750**	**100.376**	**100.096**	**100.015**	**99.929**	**99.644**	**99.248**	**99.297**	**99.662**
Cation based on 6 oxygen																										
Si	1.973	1.975	1.981	1.973	1.973	1.964	1.963	1.892	1.872	1.959	1.987	1.960	1.989	2.005	1.943	1.951	1.936	1.937	1.925	1.930	1.970	1.959	1.968	1.969	1.936	1.957
Al	0.027	0.025	0.019	0.027	0.027	0.036	0.037	0.108	0.128	0.041	0.013	0.040	0.011	0.000	0.057	0.049	0.064	0.063	0.075	0.070	0.030	0.041	0.032	0.031	0.064	0.043
ΣT	2.000	2.000	2.000	2.000	2.000	2.000	2.000	2.000	2.000	2.000	2.000	2.000	2.000	2.005	2.000	2.000	2.000	2.000	2.000	2.000	2.000	2.000	2.000	2.000	2.000	2.000
Al	0.061	0.064	0.069	0.068	0.071	0.059	0.068	0.083	0.063	0.074	0.081	0.041	0.067	0.089	0.049	0.056	0.045	0.044	0.047	0.050	0.041	0.034	0.052	0.059	0.022	0.019
Fe^{3+}	0.000	0.000	0.000	0.000	0.000	0.000	0.000	0.007	0.050	0.000	0.000	0.000	0.000	0.000	0.000	0.000	0.000	0.002	0.007	0.000	0.000	0.000	0.000	0.000	0.039	0.017
Ti	0.007	0.006	0.007	0.013	0.006	0.010	0.005	0.010	0.012	0.013	0.013	0.010	0.004	0.010	0.010	0.011	0.012	0.006	0.006	0.007	0.015	0.019	0.023	0.022	0.011	0.011
Cr	0.011	0.011	0.013	0.011	0.012	0.014	0.011	0.013	0.012	0.014	0.011	0.011	0.006	0.013	0.013	0.021	0.013	0.016	0.022	0.027	0.003	0.012	0.001	0.001	0.001	0.000
Ni	0.001	0.004	0.000	0.002	0.004	0.001	0.001	0.001	0.000	0.001	0.002	0.000	0.000	0.002	0.000	0.001	0.002	0.002	0.003	0.001	0.002	0.001	0.000	0.000	0.001	0.000
Mg	0.919	0.915	0.911	0.907	0.907	0.916	0.916	0.886	0.863	0.893	0.893	0.938	0.923	0.860	0.928	0.911	0.928	0.930	0.915	0.916	0.939	0.934	0.797	0.848	0.926	0.953
Fe^{2+}	0.000	0.000	0.000	0.000	0.000	0.000	0.000	0.000	0.000	0.000	0.000	0.000	0.000	0.029	0.000	0.000	0.000	0.000	0.000	0.000	0.000	0.000	0.127	0.070	0.000	0.000
ΣM1	**1.000**	**1.000**	**1.000**	**1.000**	**1.000**	**1.000**	**1.000**	**1.000**	**1.000**	**1.000**	**1.000**	**1.000**	**1.000**	**1.000**	**1.000**	**1.000**	**1.000**	**1.000**	**1.000**	**1.000**	**1.000**	**1.000**	**1.000**	**1.000**	**1.000**	**1.000**
Mg	0.089	0.089	0.078	0.097	0.060	0.062	0.064	0.033	0.122	0.074	0.029	0.039	0.040	0.000	0.117	0.127	0.101	0.108	0.105	0.077	0.053	0.007	0.000	0.000	0.011	0.035
Fe^{2+}	0.206	0.199	0.197	0.204	0.190	0.198	0.194	0.296	0.193	0.212	0.232	0.242	0.287	0.311	0.180	0.180	0.175	0.172	0.165	0.179	0.388	0.288	0.404	0.209	0.289	0.322
Mn	0.004	0.010	0.004	0.006	0.005	0.003	0.004	0.007	0.004	0.005	0.006	0.002	0.007	0.012	0.006	0.006	0.005	0.007	0.002	0.004	0.013	0.007	0.012	0.006	0.007	0.009
Ca	0.689	0.689	0.707	0.676	0.730	0.179	0.724	0.648	0.660	0.693	0.715	0.708	0.657	0.665	0.684	0.673	0.702	0.703	0.713	0.722	0.534	0.684	0.571	0.761	0.673	0.620
Na	0.012	0.015	0.014	0.016	0.015	0.018	0.014	0.016	0.021	0.016	0.018	0.009	0.008	0.007	0.014	0.014	0.017	0.010	0.014	0.018	0.012	0.015	0.013	0.025	0.020	0.015
ΣM_2	1.000	1.000	1.000	1.000	1.000	1.000	1.000	1.000	1.000	1.000	1.000	1.000	1.000	1.000	1.000	1.000	1.000	1.000	1.000	1.000	1.000	1.000	1.000	1.000	1.000	1.000

Table 3: Whole-rock Sm–Nd isotopic data of the basaltic rocks of the Apoteri Formation.

Sample	Lava flow	Sm (ppm)	Nd (ppm)	$^{147}Sm/^{144}Nd$	$^{143}Nb/^{144}Nd$ (±2SE)	fSm/Nd	ε_{Nd} (0)	ε_{Nd} t=0.17 Ga)	T_{Dm} (Ga)
S0 02	Ap1	4.602	18.927	0.1470	0.512455 ± 7	-0.25	-3.57	-2.56	1.33
S0 26	Ap1	4.481	18.329	0.1478	0.512464 ± 5	-0.25	-3.40	-2.36	1.33
S0 27	Ap1	4.383	18.007	0.1471	0.512446 ± 9	-0.25	-3.75	-2.58	1.35
S0 28	Ap1	4.376	17.950	0.1474	0.512456 ± 10	-0.25	-3.55	-2.51	1.33
S0 04	Ap2	2.823	11.361	0.1502	0.512399 ± 8	-0.24	-4.66	-3.71	1.53
S0 20	Ap2	3.210	13.096	0.1482	0.512374 ± 15	-0.25	-5.16	-4.17	1.54

Table 4: Whole-rock Sr–Sr isotopic data of the basaltic rocks of the Apoteri Formation.

Sample	Lava flow	$^{84}Sr/^{86}Sr$ (±2SE)	$^{87}Sr/^{86}Sr$ (±2SE)	$^{88}Sr/^{86}Sr$ (±2SE)	$^{86}Sr/^{88}Sr$ (±2SE)	Rb (ppm)	Sr (ppm)	$^{87}Rr/^{86}Sr$	$^{87}Sr/^{86}Sr$ (t=175 Ma)
S0 02	Ap1	0.056257 ± 11	0.714475 ± 4	8.762847 ± 8	0.114118 ± 1	82.91	207	1.1736	0.71155
S0 26	Ap1	0.056305 ± 8	0.711178 ± 4	8.755676 ± 9	0.114212 ±	46.4	229	0.5864	0.70972
S0 27	Ap1	0.056337 ± 6	0.711267 ± 5	8.757603 ± 8	0.114187 ± 1	34.32	231	0.4300	0.71020
S0 28	Ap1	0.056394 ± 8	0.712543 ± 4	8.770781 ± 7	0.114015 ± 1	41.4	254	0.4718	0.71137
S0 04	Ap2	0.056324 ± 8	0.714820 ± 5	8.760879 ± 6	0.114144 ± 1	65.4	343	0.5520	0.71345
S0 20	Ap2	0.056358 ± 6	0.713113 ± 4	8.755995 ± 16	0.114207 ± 2	55.2	316	0.5056	0.71185